Regionalizing the Impacts of Wind- and Wave-Induced Currents on Surface Ocean Dynamics: A Long-Term Variability Analysis in the Mediterranean Sea

Verónica Morales-márquez, Ismael Hernández-carrasco, Gonzalo Simarro, Vincent Rossi, Alejandro Orfila

Regionalizing the impacts of wind and wave-induced currents on surface ocean dynamics: a long-term variability analysis in the Mediterranean Sea

Verónica Morales-Márquez[1], Ismael Hernández-Carrasco[1], Gonzalo Simarro[2], Vincent Rossi[3], Alejandro Orfila[1]

[1]Mediterranean Institute for Advanced Studies (CSIC-UIB), Miquel Marquès, 21, 07190, Esporles, Illes Balears, Spain
[2]Institut de Ciències del Mar-CSIC, Passeig Marítim de la Barceloneta, 37-49, 08003, Barcelona, Spain
[3]Mediterranean Institute of Oceanography (CNRS), 13288 Marseille, France

Key Points:

- Dynamically coherent regions in the Mediterranean are defined based on the Ekman, Stokes and geostrophic components variability.
- Ageostrophy dominates surface circulation short-term variability and exceed geostrophy over Northwest Mediterranean Sea in winter.
- Variations in the kinetic energy correlate well with the main Mediterranean climate modes in regions dominated by Ekman and Stokes.

Corresponding author: Verónica Morales-Márquez, vmorales@imedea.uib-csic.es

This article has been accepted for publication and undergone full peer review but has not been through the copyediting, typesetting, pagination and proofreading process, which may lead to differences between this version and the Version of Record. Please cite this article as doi: 10.1029/2020JC017104.

Abstract

Effects of wind and waves on the surface dynamics of the Mediterranean Sea are assessed using a modified Ekman model including a Stokes-Coriolis force in the momentum equation. Using 25 years of observations, we documented intermittent but recurrent episodes during which Ekman and Stokes currents substantially modulate the total mesoscale dynamics by two non-exclusive mechanisms: (i) by providing a vigorous input of momentum (e.g. where regional winds are stronger) and/or (ii) by opposing forces to the main direction of the geostrophic component. To properly characterize the occurrence and variability of these dynamical regimes we perform an objective classification combining self-organizing maps (SOM) and wavelet coherence analyses. It allows proposing a new regional classification of the Mediterranean Sea based on the respective contributions of wind, wave and geostrophic components to the total mesoscale surface dynamics. We found that the effects of wind and waves are more prominent in the northwestern Mediterranean, while the southwestern and eastern basins are mainly dominated by the geostrophic component. The resulting temporal variability patterns show a strong seasonal signal and cycles of 5 - 6 years in the total kinetic energy arising from both geostrophic and ageostrophic components. Moreover, the whole basin, specially the regions characterized by strong wind- and wave- induced currents, shows a characteristic period of variability at 5 years. That can be related with climate modes of variability. Regional trends in the geostrophic and ageostrophic currents shows an intensification of $0.058 \pm 1.43 \cdot 10^{-5}$ cm/s per year.

Plain Language Summary

The ocean dynamics plays a decisive role in the global balance of essential variables, such as heat, CO2 or primary production, as well as in the dispersion of pollutants. However, the physical processes that control the mesoscale dynamics and its variability in the surface of the Mediterranean sea is not fully understood. Therefore, we have analyzed the regional contribution of the geostrophic and the wind and waves induced currents using a classification method based on a machine learning algorithm. We find that the effect of wind and waves is stronger over regions of the northwestern Mediterranean, while the southwestern and eastern basin is mainly dominated by geostrophy. We observe that regions where wind and wave dominate the dynamics co-vary with the main Mediterranean climate modes of variability. The geostrophic currents show an intensification with a clear shift in 2002, which suggests that this positive trend could be a part of a large decadal oscillation.

1 Introduction

Ocean currents are of crucial importance for the transport of physical, chemical and biological variables across the world oceans. They are the main responsible for the horizontal redistribution of energy, salt and heat, playing an important role in the climate system (Covey & Barron, 1988). In particular, the sea surface is a key transitional layer where most biological and biogeochemical activities concentrate and tightly interact with vigorous physical features (e.g. Hernández-Carrasco et al., 2014) ultimately affecting marine biodiversity patterns (e.g. Villarino et al., 2018) and atmosphere-ocean coupled processes (e.g. Bronselaer & Zanna, 2020). Hence, a precise knowledge of the circulation in the upper oceanic boundary layer and of its variability is key to many issues of broad scientific and practical importance, ranging from ecosystem and fisheries management (e.g. Dubois et al., 2016; Futch & Allen, 2019), the tracking of marine pollution including microplastic (e.g. Van Sebille et al., 2015) to marine safety such as search and rescue operations (e.g. Sayol et al., 2014).

Oceanic circulation results from movements of fluid in response to internal forces (pressure gradients and Coriolis forces) and external forces (gravity forces and frictional

forces, such as wind stress and waves at the surface and drag at the bottom and lateral boundary layers). At the ocean surface, total currents result from several energy inputs from diverse sources occurring at multiple scales. In particular, wind and waves interact with the ocean general circulation, giving rise to a highly variable multi-scale environment. During the last decade or so, mesoscale surface currents have traditionally been interpreted as dominated by the geostrophy. This simplifying assumption, together with the advances in satellite altimetry, have led the oceanographic community to estimate surface horizontal currents from the balance between the pressure gradient and the Coriolis forces. However, although geostrophy provides a reasonable view of the low frequency/large-scale motion of the ocean, it has limitations. As such, previous studies aimed at expressing total currents as a sum of both geostrophic and Ekman components (Sudre et al., 2013; Rio et al., 2014). Despite relative improvements, our description of the upper oceanic layer dynamics is still incomplete as it is also necessary to account for the high frequency and ageostrophic motions caused by both wind- and wave-driven currents. Indeed, there is growing evidence that the mesoscale ageostrophic flow plays an important role in the transport and mixing processes, affecting the distribution patterns of transported materials (Dobler et al., 2019) such as, the fate of marine debris (Onink et al., 2019). Moreover, Fraser et al. (2018) have shown that wave-induced currents enhance ocean connectivity around Antarctica, potentially affecting the local ecosystems.

Although great advances have been made in the last decades for measuring geostrophy at meso and larger scales or wind stress over the ocean surface, such as satellite scatterometers like QuikSCAT or ASCAT (Bourassa et al., 2019), wave and wind-wave combined measurements are still limited to specific sites (mooring, stations and buoys) or interpolated from radar radiometers (Ardhuin et al., 2018). However, the availability of global forecasting systems both for wave and surface winds, allows the inclusion of these high frequency velocities in recently developed models of the ocean circulation, by merging the different sources to obtain improved velocity products (Breivik et al., 2016; Onink et al., 2019).

The wind-driven currents at the sea surface were initially studied by Ekman's seminal work (Ekman, 1905). He proposed that the momentum balance between the turbulence stress caused by the wind and Coriolis force can be modeled as a classical diffusion problem but with a kinematic viscosity. Besides, gravity waves have an associated current, the Stokes velocity resulting from the non-linearity of the wave orbital velocities (Stokes, 1847). From the Eulerian standpoint, the Stokes-drift-induced-current component acts as an additive term that interacts with the mean ageostrophic current, appearing in the momentum equations as an external force such as, a vortex force or as the Coriolis-Stokes force (McWilliams & Restrepo, 1999; Polton et al., 2005). The low and high frequency velocities can be of the same order of magnitude depending on the intensity of the local wind and wave fields (Polton et al., 2005; Breivik et al., 2016; Fraser et al., 2018).

Despite substantial efforts in studying the effects of wind and waves on surface currents around the world (Kaiser, 1994; Polton et al., 2005; Ardhuin et al., 2009; Hui & Xu, 2016; Onink et al., 2019), our knowledge of these ageostrophic currents and of their impacts on the upper layer dynamics of the Mediterranean Sea is still poor. The Mediterranean Sea is a semi-enclosed basin with large spatial and seasonal variability of both winds and wave fields, making it an excellent laboratory to study the effects of the interaction of the wind and wave induced currents in the general circulation. Sayol et al. (2016) studied the energy and mass fluxes generated by wind-wave interactions in the western part of the Mediterranean Sea and showed, that the induced surface transport has a seasonal character, peaking during winter seasons. Recently, Morales-Márquez et al. (2020) showed that this variability is largely controlled by large-scale climatic patterns. The atmospheric circulation over the Mediterranean Sea can be indeed characterized by specific modes of variability related to atmospheric teleconnections (Wallace

& Gutzler, 1981). The main climatic patterns influencing the Mediterranean dynamics are the North Atlantic Oscillation (NAO), the East Atlantic pattern (EA), the Scandinavia pattern (SCAND) and the East Atlantic/Western Russia (EA/WR) (Barnston & Livezey, 1987; Morales-Márquez et al., 2020).

In this paper, we first derive analytical expressions to estimate the total oceanic surface currents as a sum of a geostrophic term and another ageostrophic one, taking into account wind and waves forcings. We then apply our expressions to altimetric and reanalyses datasets in order to compute surface currents over the whole Mediterranean Sea for the last 25 years. It allows investigating the relative contributions, which vary in space and time, of both geostrophic and ageostrophic components to the total kinetic energy. In order to identify the regions where the Ekman- and Stokes-induced flows affect substantially the upper ocean dynamics, we perform an objective regionalization of the Mediterranean Sea. Homogeneous dynamical regions are unveiled using a machine-learning algorithm applied to an artificial neural network. Previous studies have proposed diverse objective regionalizations of the Mediterranean Sea (Ayata et al., 2018), using different statistical techniques, and based on different oceanic variables, e.g. climatological averages of temperature, salinity, nutrients concentrations (Reygondeau et al., 2017), transport properties of surface waters (Rossi et al., 2014) or phytoplankton variability (d'Ortenzio & d'Alcalà, 2009; Nieblas et al., 2014). By doing so, we analyze the regional variability of the dynamical impacts of both winds and waves on the surface circulation in the Mediterranean Sea. In each homogeneous dynamical region, we further extract the dominant temporal scales and study their relationships with the main climatic modes to assess the interannual variability of the currents field.

2 Sea Surface Currents

Total current at the sea surface ($\mathbf{U_t}$) can be expressed as the sum of the geostrophy, $\mathbf{U_g} = u_g + iv_g$, and an ageostrophic velocity, $\mathbf{U_a} = u_a + iv_a$ which is associated with the wind and non linear wave-induced momentum along their direction of propagation:

$$\mathbf{U_t} = \mathbf{U_g} + \mathbf{U_a}. \tag{1}$$

2.1 Geostrophic currents

Considering a steady and Boussinesq flow, the geostrophic term can be obtained from the equilibrium between Coriolis and pressure gradient forces in the momentum equation:

$$\mathrm{i}f\mathbf{U_g} = -\frac{1}{\rho_w}\nabla P, \tag{2}$$

where $\nabla = \frac{\partial}{\partial x} + i\frac{\partial}{\partial y}$ and P is the pressure. Using the hydrostatic balance in homogeneous ocean, an expression of the geostrophic velocities can readily be obtained from the Sea Surface Height (SSH) as:

$$u_g = -\frac{g}{f}\frac{\partial(\mathrm{SSH})}{\partial y}, \quad v_g = \frac{g}{f}\frac{\partial(\mathrm{SSH})}{\partial x}, \tag{3}$$

where g is the acceleration of gravity and $f = 2\Omega sin\phi$ is the Coriolis parameter with Ω the angular Earth velocity and ϕ the latitude.

2.2 Ageostrophic currents: wind and wave driven components

The wind- and wave-induced ageostrophic currents in the upper boundary layer are obtained from the horizontal Ekman-wave induced momentum equation for a steady and

Boussinesq flow (Lewis & Belcher, 2004; Huang, 1979; Polton et al., 2005):

$$\mathrm{i}f\mathbf{U_a} = \frac{\partial}{\partial z}\left(\mathrm{A}_z \frac{\partial \mathbf{U_a}}{\partial z}\right) - \mathrm{i}f\mathbf{U_s}, \tag{4}$$

where $\mathbf{U_a} = u_a + iv_a$ denotes the horizontal ageostrophic velocity in complex notation, $\mathbf{U_s} = u_s + iv_s$ is the wave-induced Stokes velocity, resulting $if\mathbf{U_s}$ the term from the Coriolis-Stokes force (rotation acting on the Stokes drift), and A_z is the vertical eddy viscosity of sea water. Previous works (Huang, 1979; Polton et al., 2005) have shown that the flow is significantly modified by the Coriolis–Stokes force not only at the near-surface layer but throughout the entire Ekman layer. We assume that the vertical viscosity is constant and equal to $A_z = 1.0710^{-2}\mathrm{m}^2\,\mathrm{s}^{-1}$ (McWilliams et al., 1997). While other approaches considered a vertical parametrization of A_z (Wenegrat & McPhaden, 2016; Polton et al., 2005), we use a constant value since: (i) it would only affect the estimation at the surface boundary condition and, (ii) the wave-induced circulation changes are independent of the vertical mixing parametrizations when the typical depth scale of the waves effect is smaller than the typical Ekman layer.

Assuming a monochromatic wave field propagating in deep water with a wavenumber $\mathbf{k} = (k_x, k_y)$, the Stokes drift velocity, $\mathbf{U_s} = U_s\widehat{\mathbf{k}}$, is related to the wave as (Phillips, 1966):

$$U_s = a^2\omega k e^{2kz}, \tag{5}$$

being a the wave amplitude, $\omega = \sqrt{gk}$ the wave frequency at deep waters, $k = |\mathbf{k}|$ and the wave number unit vector:

$$\widehat{\mathbf{k}} = \cos\left(\theta_\mathrm{w}\right) + \mathrm{i}\sin\left(\theta_\mathrm{w}\right), \tag{6}$$

with θ_w the mean direction of propagation waves, which is not necessarily parallel to the wind stress.We compute the Stokes including the sea and swell components of the wave. Thus, the combined effect of wind and waves are not only provided in the generation area but also while waves propagate across their swell.

Both boundary conditions required by the second-order ordinary differential equation (Eq. 4) are given at the free surface and at the vanishing boundary as:

$$\mathrm{A}_z\frac{\partial \mathbf{U_a}}{\partial z} = \frac{1}{\rho_w}\left(\boldsymbol{\tau} + \frac{\partial \boldsymbol{S}}{\partial \boldsymbol{X}}\right), \qquad \text{at} \qquad z = 0, \tag{7}$$

$$\mathbf{U_a} \to 0, \qquad \text{as} \qquad z \to -\infty, \tag{8}$$

where ρ_w the sea water density and $\boldsymbol{\tau}$ is the wind stress at the sea surface, $\boldsymbol{\tau} = \rho_a C_D u_{10}\mathbf{u_{10}}$, where ρ_a is the air density (1.2 kg/m^3, u_{10} is the 10-m wind speed and C_D is the neutral drag coefficient taken as, $C_D = (2.7/u_{10}+0.142+0.0764u_{10})/1000$ following Large et al. (1994). S_{ij} are the components of the radiation stress provided at the surface by:

$$\frac{\partial \boldsymbol{S}}{\partial \boldsymbol{X}} = \left(\frac{\partial S_{xx}}{\partial x} + \frac{\partial S_{yx}}{\partial y}\right) + i\left(\frac{\partial S_{xy}}{\partial x} + \frac{\partial S_{yy}}{\partial y}\right),$$

$$S_{xx} = \frac{E}{2}\cos^2\theta_\mathrm{w}, \quad S_{xy} = S_{yx} = \frac{E}{2}\sin\theta_\mathrm{w}\cos\theta_\mathrm{w}, \quad S_{yy} = \frac{E}{2}\sin^2\theta_\mathrm{w},$$

with $E = \rho g a^2/2$.

The steady-state solution of Eq. 4 subjected to boundary conditions (Eq. 7-8) is:

$$\mathbf{U_a}\left(z\right) = \frac{\boldsymbol{\tau}}{\rho_w \mathrm{A}_z m}e^{mz} + \frac{\frac{\partial \boldsymbol{S}}{\partial \boldsymbol{X}}}{\rho_w \mathrm{A}_z m}e^{mz} + \frac{m^2\mathbf{U_{s0}}}{4k^2 - m^2}e^{2kz} - \frac{2km\mathbf{U_{s0}}}{4k^2 - m^2}e^{mz}, \tag{9}$$

with $\mathbf{U_{s0}} = \mathbf{U_{s(z=0)}}$, $m = \sqrt{\mathrm{i}f/\mathrm{A}_z} = (1+\mathrm{i})\,\lambda$ and $\lambda = \sqrt{f/\left(2\mathrm{A}_z\right)}$. The characteristic depth of the Ekman layer is defined as $\delta_e = 1/m$ and the characteristic Stokes depth scale as $\delta_s = 1/2k$.

To clarify the importance Coriolis-Stokes interaction, Eq.9 is rewritten as,

$$\mathbf{U_a}\,(z) = \mathbf{U_E}\,(z) + \mathbf{U}_{\tau_\mathbf{w}}\,(z) + \mathbf{U_S}\,(z) + \mathbf{U_{ES}}\,(z)\,. \tag{10}$$

Each term constituting Eq. 10 corresponds to the different components of the ageostrophic velocity. $\mathbf{U_E}\,(z)$ represents the classical Ekman component. $\mathbf{U}_{\tau_\mathbf{w}}\,(z)$ accounts for the surface current induced by the wave radiation stress, which will not be analyzed separately in the following sections because its value is small compared to the other components, $\mathbf{U_S}\,(z)$ is the Stokes component, that decreases over the Stokes depth scale, being much shallower than the Ekman layer ($\delta_s \ll \delta_e$). The latter component is correlated with the dynamical response to the Coriolis–Stokes force, being different than the Lagrangian Stokes drift U_s given by Eq. 5. The last term, $\mathbf{U_{ES}}\,(z)$ is the Ekman-Stokes component that accounts for the non-linear interaction between wind and waves acting over the entire Ekman layer (Polton et al., 2005).

Here, $\mathbf{U_a}$ is integrated over 1 meter depth since the mean Stokes layer depth is generally smaller than 2m in the Mediterranean Sea (Sayol et al., 2016). Fig. 1 displays an example of the vertical distribution of the Stokes (red arrows), Ekman (blue arrows) and ageostrophic (black arrows) velocity components along the water column in the Mediterranean Sea. It clearly shows that the Stokes component has a smaller influence (only a few meters near sea surface), while the Ekman component has a significant effect at deeper depths. Also, it is important to note how the Stokes component modify the vertical distribution of the ageostrophic velocities in spite of its relative small value as compared to the Ekman velocity (see the difference between blue and black arrows).

The velocity fields obtained with this formulation have been validated with the drifters-database provided by the National Institute of Oceanography and Experimental Geophysics Institute (OGS) of Italy. This data encompasses drifters in the Mediterranean Sea from 1986 to 2016. The averaged separation distance between the real and the virtual drifter trajectories averaged over all the hourly initializations is smaller (up to 15 km smaller after 72 hours of integration, not shown) when the virtual drifter trajectory is computed using the total velocity field as compared to the geostrophic velocities. Besides, we found that the variance of the difference between the virtual and the real drifters is also smaller when we advect the drifters in the total velocity field, showing that errors in $\mathbf{U_T}$ are significantly reduced as compared to $\mathbf{U_g}$.

Further modifications of the Ekman model have been considered in the last years, such as including an additional ageostrophic component caused by the geostrophic stress (McWilliams et al., 2015; Wenegrat & McPhaden, 2016). The global comparison between the different ageostrophic components performed in Wenegrat and McPhaden (2016) shows that this term has a higher influence at low latitudes while the Coriolis-Stokes stress dominates at higher latitudes, as in the case of the Mediterranean Sea. Additionally, in the very surface layers of the ocean this component (geostrophic stress) has not a significant value on the effective stress profile, and a relative value respect to the surface wind stress smaller than 3% in spring and summer and smaller than 8% in winter and autumn over the Mediterranean Sea, as shown in Figure 9 of Wenegrat and McPhaden (2016). They also found that the contribution of Coriolis-Stokes stress is 5 times greater than the geostrophic stress in the Mediterranean Sea, with a seasonal variability significantly larger in the Coriolis-Ekman induced currents. This small contribution suggests that the results obtained in this study will not be substantially modified if the geostrophic stress is considered in the Mediterranean basin.

3 Data

3.1 Wave and atmospheric data

Gridded wave and sea surface wind data can be obtained from remote sensing equipped with scatterometer (Bourassa et al., 2019) and from model outputs. However, while satel-

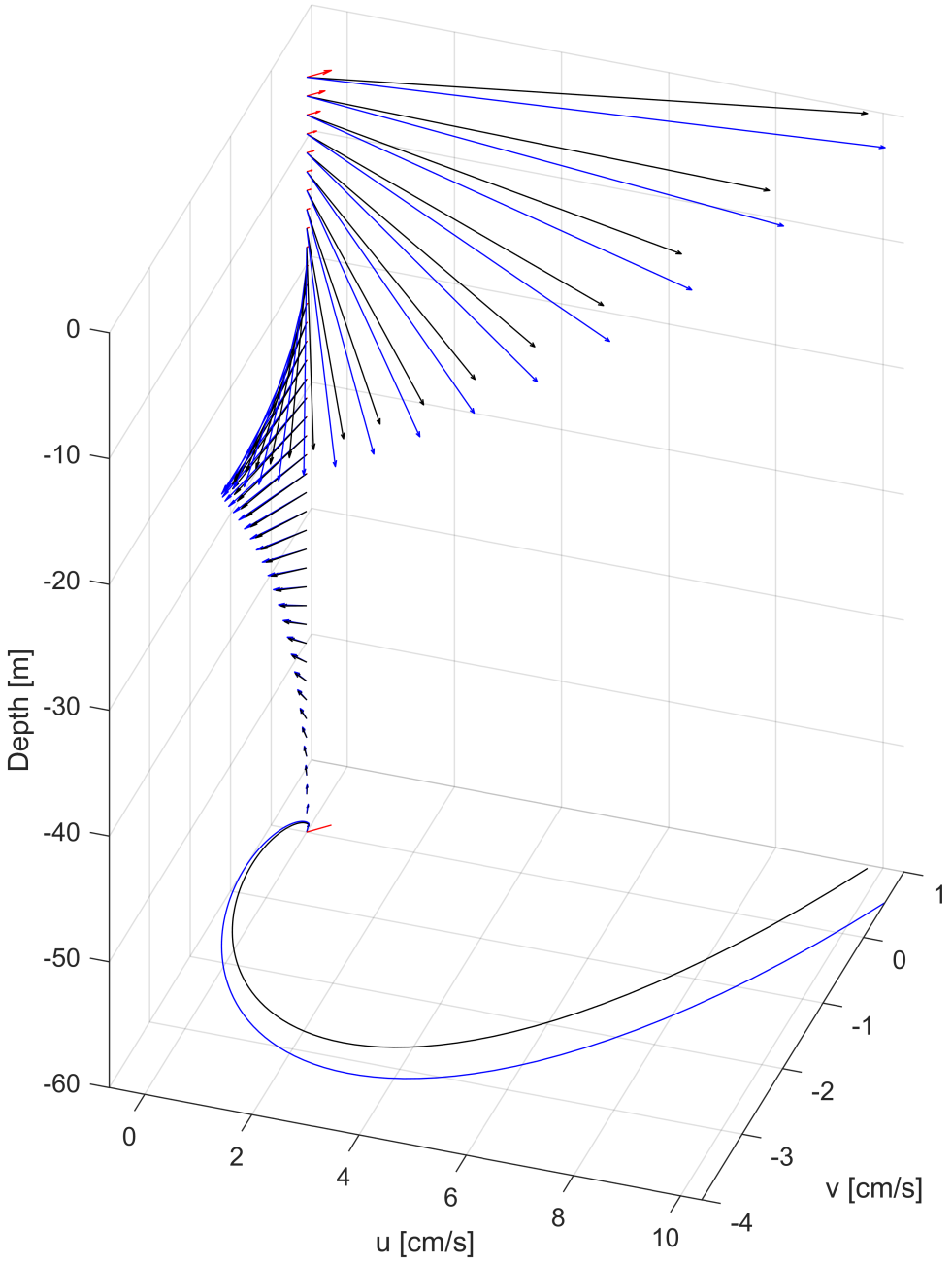

Figure 1. Ekman (blue line), Stokes (red line) and ageostrophic (black line) velocity profiles at spatial point 6°E, 38.5°N corresponding to the 5th of February 2014 at 6 : 00 UTC.

Table 1. Statistical comparison between the ERA-Interim and ERA5 dataset.

Variable	R^2	SCI	RB
SWH	0.96	0.20	−0.04
U_{10}	0.90	0.42	−0.01
V_{10}	0.89	0.44	−0.05

lites collect indirect observations of wind and waves (Ardhuin et al., 2018), data are acquired along tracks, generating maps with an effective resolution of approximately 40-50km and one week. Since the wave field changes at high frequency, that is for periods spanning a few hours, remote-sensed winds are not the most suitable dataset in order to study the wave effect on surface circulation. Concurrently, there exist nowadays consistent and global database about the wave field, also providing high-resolution wind velocities, that are generated by model reanalyses. Such model reanalyses have been extensively validated with different *in-situ* observations (Berrisford et al., 2011) and have already been used to study transport in the ocean (Breivik et al., 2016).

Surface waves and 10-m above the sea surface wind velocities are provided by the ERA-Interim reanalysis (Dee et al., 2011). Wave fields are obtained using the WAM wave model with the assimilation of available global measurements of ERS1 wave height data (Janssen et al., 1997). These reanalysis data are provided by local GRIB code of the European Centre for Medium-Range Weather Forecasts (ECMWF) covering the period between 1979 and 2019 with a temporal resolution of 6 hours and a spatial resolution of 0.125° both in latitude and longitude in the Mediterranean Sea (Fig. 2). For a detailed description of these products the reader is referred to Berrisford et al. (2011).

While new wind and wave reanalysis are currently available in the Mediterranean Sea, we use ERA Interim since it provides wind and wave fields at a spatial resolution consistent with the geostrophic velocity field; i.e. 0.125° in the Mediterranean Sea against 0.25° of winds provided by ERA5, and even coarser for the wave field (0.5° against 0.125° of ERA-Interim). Furthermore, we have compared both products and we have found a high correlation and low values of Scatter index and Relative bias between both reanalysis data, as shown in Table 1 (Roelvink et al., 2009).

The leading climatic modes of variability in the Mediterranean Sea, NAO, EA, EA/WR and SCAND have been downloaded from the NOAA Climate Prediction Centre (`https://www.cpc.ncep.noaa.gov/data/teledoc/telecontents.shtml`; last access on: 27 February 2020). NAO is usually defined as the sea level pressure difference between the Iceland Low and the Azores High (Hurrell et al., 2003). The EA index consists of a north-south dipole of anomaly over the North Atlantic, with a strong multidecadal variability. The EA/WR is represented with four main anomaly centers; positive phase is associated with positive wave height anomalies located over Europe and negative wave height anomalies over the central North Atlantic. Finally the SCAND pattern is composed with a primary circulation center over Scandinavia, with weaker centers of opposite sign over western Europe. Climate indices are constructed through a rotated principal component analysis of the monthly mean standardized 500-mb height anomalies in the Northern Hemisphere, ensuring the independence between modes at a monthly scale due to orthogonality (Barnston & Livezey, 1987).

3.2 Geostrophic velocity field

Geostrophic currents are derived from the Sea Level Anomaly (SLA) provided by the Copernicus Marine Environment Monitoring Service (CMEMS) through the product *Mediterranean Sea Gridded L4 Sea Surface Heights and derived variables reprocessed*

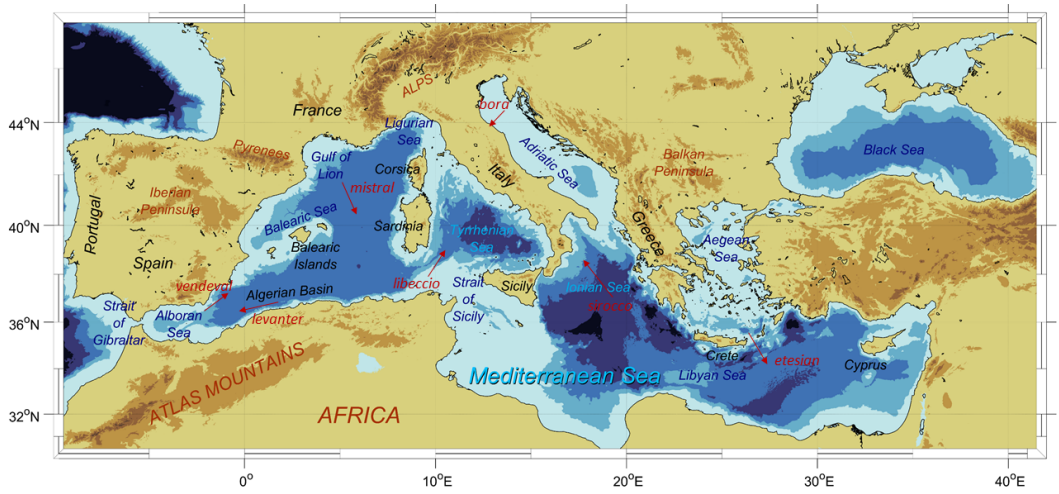

Figure 2. Topography of the Mediterranean basin and naming convention of the main geographical locations used in the paper.

(1993-ongoing) (`https://resources.marine.copernicus.eu/?option=com_csw&view=details&product_id=SEALEVEL_MED_PHY_L4_REP_OBSERVATIONS_008_051`; last access on: 7 February 2019). This product merges the different altimeter missions available (Jason-3, Sentinel-3A, Haiyang-2A, Saral/AltiKa, Cryosat-2, Jason-2, Jason-1, TOPEX/Poseidon, ENVISAT, GFO, ERS1/2). SLA data are homogenized by the DUACS multimission altimeter data processing system in order to generate gridded L4 absolute geostrophic velocities and optimal reprocessed products for long-term analysis, including the robust estimation of regional mean sea levels trends (Pujol et al., 2016). This data set has a daily temporal resolution and is provided over a regular mesh of 0.125° over the entire Mediterranean Sea.

Velocity fields $\mathbf{U}_g$ and $\mathbf{U}_a$ are computed every 6 hours for 25 years from 1993 to 2018. For the geostrophic component, daily data are linearly interpolated to 6-hourly time step, while for the ageostrofic component, each of the terms are computed for each model output.

4 Statistical Methods

4.1 Self Organizing Maps

Self-Organizing Maps (SOMs) is a statistical method using unsupervised learning neuronal network which is especially suited to extract patterns in large datasets (Kohonen, 1982). SOM is a nonlinear mapping tool that reduces the high-dimensional feature space of the input data to a lower dimensional (usually 2D) network of units called neurons. Through the machine learning algorithm, SOMs are able to compress the information contained in large and complex dataset into a single set of patterns. Similar neurons are mapped adjacent on the network, since SOM preserves topology. This helps to improve the visualization of the patterns, being one of the advantages of this technique.

SOM learning process algorithm inserts the input velocity fields into a neural network which is modified along an iterative procedure. Each neuron is represented by a

weight vector containing as many components as the dimension of the input sample data. At each iteration, the neuron whose weight vector is closest (as measured by minimum Eulerian distance) to input data vector is retrofitted together with its topological neighbors towards the input sample according to a neighborhood relationship specified with a given mathematical function. At the end of the training process, SOM approximates the probability density function of the input data associating each neuron with a reference pattern.

The SOM technique is able to be applied both in the spatial and temporal domains. Since we are interested in classifying the regions in the Mediterranean Sea according to the temporal variability of each of the velocity components, we implement SOM analysis in the time domain. The input data set is constituted not only by the total velocity time-series ($\mathbf{U_T}$) at each grid point, but also by coupling the geostrophic ($\mathbf{U_g}$), Ekman ($\mathbf{U_E}$) and Stokes ($\mathbf{U_S}$) velocities at the same grid point; as such, it allows analyzing the simultaneous variations of these terms. The resulting time-series are normalized before starting the learning process. At its completion, each neuron will correspond to a specific velocity temporal pattern for $\mathbf{U_T}$, $\mathbf{U_g}$,$\mathbf{U_E}$ and $\mathbf{U_S}$. Then, the time-series of the velocity components at each grid point are classified in accordance with the SOM temporal patterns, providing a map of different sub-regions characterized with a particular temporal variability. To compromise the levels of the regionalization and its interpretability, we retain 6 neurons (2x3 SOM) for the temporal analysis. Preliminary tests using larger numbers of neurons returned more detailed temporal patterns for numerous sub-regions which are, however, difficult to clearly distinguish by their dynamical behaviors (see the supplementary material Fig. A1, Fig. A2 and Hernández-Carrasco and Orfila (2018)). We use a hexagonal map lattice in order to have equidistant neighbors and do not introduce artificial anisotropy. We opted for a linear mode for the initialization, a batch algorithm for the training process, and an 'ep' type of neighborhood function since this parameter configuration produces lower quantitative and topological errors and a minimize computational cost (Liu et al., 2006).

4.2 Wavelet power spectral method

Wavelet transform of a time-series x_n ($W^X(s)$) performs a time-frequency domain decomposition of the time-series by varying the wavelet scale s and by estimating its spectral characteristics as a function of time (Torrence & Compo, 1998). Wavelet is able to extract local-frequency information from a temporal signal in order to extract the dominant modes of variability and detect changes over time (Torrence & Compo, 1998). Wavelet uses a Fourier transform approach on a sliding temporal window returning frequencies at each time step, therefore being well suited for identifying periodic phenomena with changing spectra (Kaiser, 1994). This tool facilitates the study of time-series that contain non-stationary power at many different frequencies (Daubechies, 1990), as is the case here. We used a Morlet wavelet transform, which is a plane wave of wavevector ω_0 modulated by a Gaussian of unit width with an adimensional frequency ω_0=6 (i.e. it contains 6 complete cycles of the temporal scale that is being analyzed). This wavelet base function is adequate to be localized in both time and frequency spaces and therefore to properly assess changes in the wavelet amplitude over time (Torrence & Compo, 1998). To distinguish the signal from the underlying noise, a threshold above the 95% confidence interval of a red-noise spectrum was used. The ability of wavelets to extract significant frequencies in localized time periods provides a powerful tool to characterize the patterns resulting from the previously-described SOMs analysis in the time domain.

4.3 Combined SOM-Wavelet coherence analysis

To assess the response of the sub-regions identified by the SOMs to large-scale forcing, we use an approach based on the Wavelet Coherence Analysis (WCA) between two time-series (Grinsted et al., 2004). WCA characterizes cross-correlations by identifying

the main frequencies, phase differences and time periods over which the relationships between the variability of the currents components (geostrophy, Ekman and Stokes) and the main relevant large-scale forcing (e.g. NAO, EA, EA/WR and SCAND indices) are tight in each region. To do so, we first analyze the variability in both frequency and time of each velocity components characteristic time and the time series of the climate indices, using the continuous wavelet transform.

Using the cross-Wavelet Transform (XWT), we determine the cyclic changes of the velocity components and their relationship with the climatic indices described above, in each of the sub-regions. The XWT of two time-series x_n and y_n indicates common power and relative phase in the frequency-time domain, given by $W^{XY}(s) = W^X(s)W^{Y^*}(s)$, where $*$ represents the complex conjugate. $|W^{XY}(s)|$ is the cross-wavelet power and the complex argument $\arg(W^{XY}(s))$ is the relative phase between both time-series (shown in the Fig. 10 as arrows).

Finally the degree of coherence of the XWT at each time point is obtained by computing the coefficient R^2 given by the squared absolute value of the smoothed cross-wavelet spectrum, normalized by the product of the smoothed wavelet squared individual spectra, for each scale (Torrence & Compo, 1998; Grinsted et al., 2004), as:

$$R_n^2 = \frac{|S(s^{-1}W_n^{XY}(s))|^2}{S(s^{-1}|W_n^X(s)|^2)S(s^{-1}|W_n^Y(s)|^2)}, \tag{11}$$

whose values range from 0 (no correlation) to 1 (perfect correlation) and where S denotes the smoothing operator along the wavelet scale axis and along time. R^2 can be interpreted as a localized correlation coefficient in the frequency-time domain. It should be noted that while cross-wavelet analysis does not establish causative relationships, still allows identifying possible linkages between variables through the synchrony of their time-series.

Last but not least, wavelet coherent analysis is particularly suited to unveil regional relationships between global forcing (climate modes of variability) and the temporal velocity patterns obtained from the SOM given its ability to extract the frequencies and time periods when two time-series are correlated, wavelet coherent analysis is particularly suited to unveil regional relationships between global forcings (climate modes of variability) and the temporal velocity patterns obtained from the SOM.

5 Results and discussion

The overall picture of the mesoscale dynamics at the upper layer is mainly dominated by the geostrophic component for most space and time windows considered (not shown). However we found time periods where the ageostrophic velocities associated with wind and waves effects largely govern the main circulation over different regions of the Mediterranean Sea. As an example, Fig. 3 shows the total surface current and its respective components for the 19$^{\text{th}}$ of January 2005 at 12 : 00 UTC. It exemplifies a dynamical situation characterized by the net prevalence of Stokes and Ekman-induced velocities compared to the geostrophic component. At the geographical coordinate N38° E7°, 37′, 30″ (i.e. central location of the south-western Mediterranean basin), the maximum values of Stokes velocity reaches 15cm/s, being the Ekman velocity of 78cm/s which is largely exceeding the geostrophic velocity of 18cm/s. The contributions of $\mathbf{U}_S$ and $\mathbf{U}_E$ to the total velocity at this location for that particular date are 16.7% and 85.18%, respectively. As shown in Fig. 3, the spatial distributions of the ageostrophic velocities between the eastern and western basins clearly differ. While in the western Mediterranean, the total velocity is mainly governed by the Ekman component (i.e. intense winds blowing in the Gulf of Lion towards the center of the basin and modifying the Northern Current), the eastern Mediterranean basin is mainly governed by geostrophy (see Fig. 2 for the distinct hydrodynamical features).

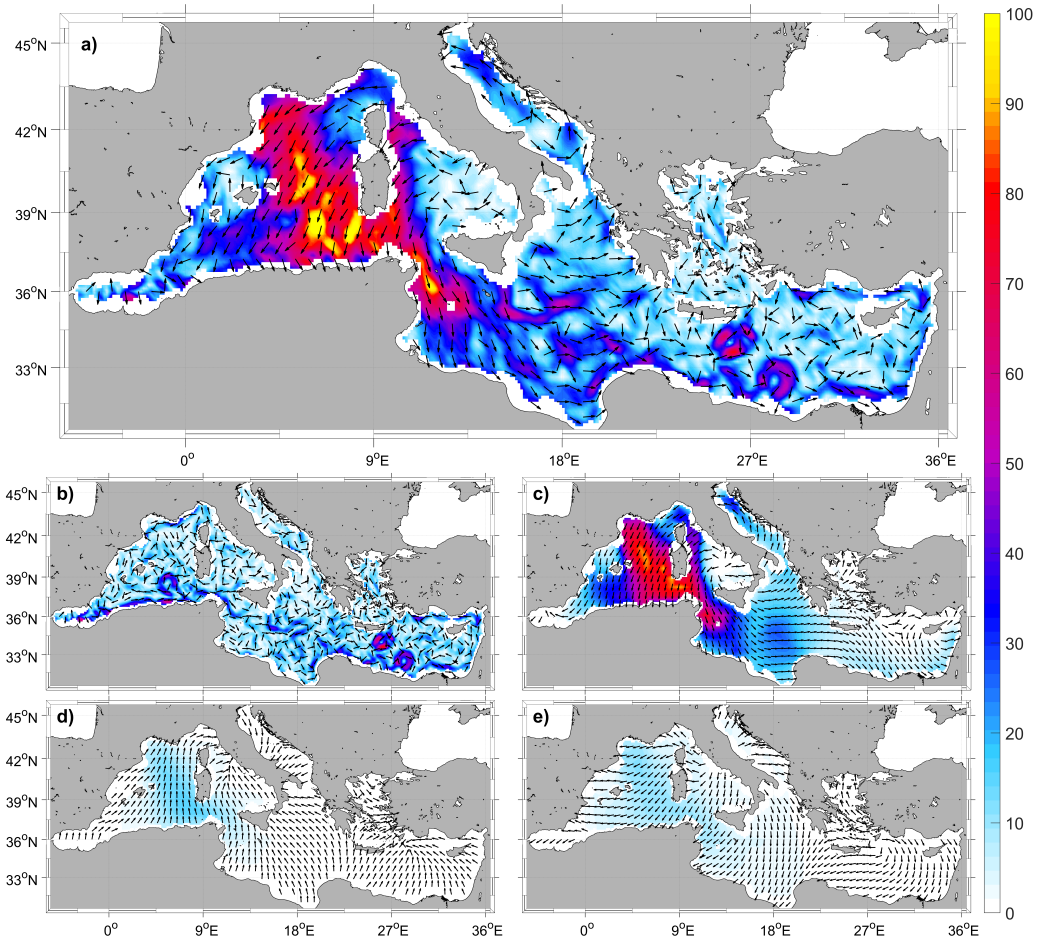

Figure 3. a) Total, b) Geostrophic, c) Ekman, d) Stokes and e) Ekman-Stokes velocity fields for January, 19th of 2005 at 12 : 00 UTC. The magnitudes (module, in cm/s) of each velocity component are displayed as background colors according to the color-scale. The black arrows represent the direction of the velocity fields. Only 1 of each 5 data points have been plotted for clarity.

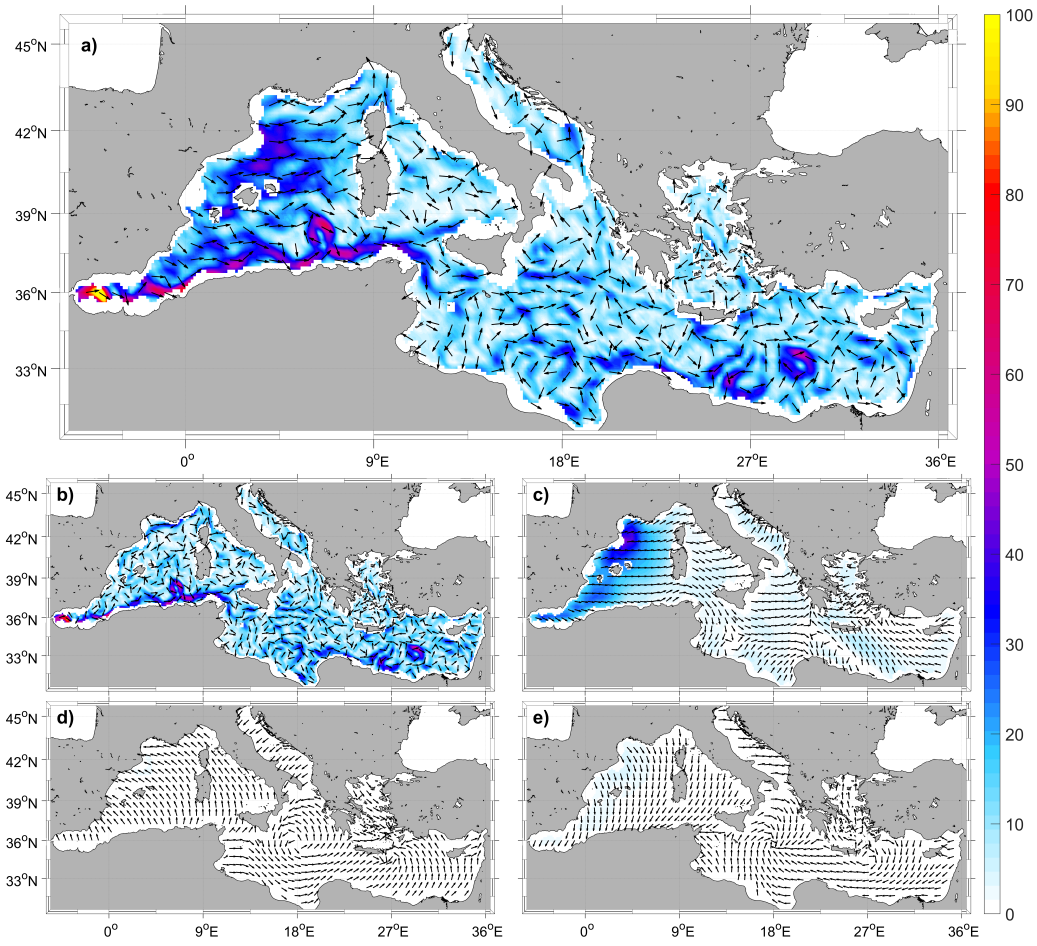

Figure 4. a) Total, b) Geostrophic, c) Ekman, d) Stokes and e) Ekman-Stokes velocity fields for February the 5th of 2014 at 6:00 UTC. The magnitudes (module, in cm/s) of each velocity component are displayed as background colors according to the color-scale. The black arrows represent the direction of the velocity fields. Only 1 of each 5 data points have been plotted for clarity.

The relevance of both Ekman and Stokes components on the total current is not only restricted to the situations where they reach maximum values, as shown by the previous exemplary case (Fig. 3), since they can also have a noticeable impacts on the dynamics with relatively small values. Indeed, the relative differences of direction between the wind stress and wave propagation on one hand, and the geostrophic component on the other hand, affect the total surface circulation. Fig. 4 displays an example corresponding to the 5th of February 2014 at 6 : 00 UTC where, even though the geostrophy represents the main contribution on the total velocity, both Ekman and Stokes components suppress the Liguro-Provençal Current (Fig. 5). This suppressor effect of the Ekman component is not caused by its intensity, ($|\mathbf{U_E}|$ is similar to $|\mathbf{U_g}|$), but because its direction is opposite to the geostrophic current direction.

It is worth noting that $\mathbf{U_{ES}}$ ensures that the total velocity satisfies the wind stress boundary condition at the sea surface. Thus, it removes the sea surface stress caused by the Stokes component ($\mathbf{U_S}$) (Polton et al., 2005; Pearson, 2018). For this reason, $\mathbf{U_S}$ and

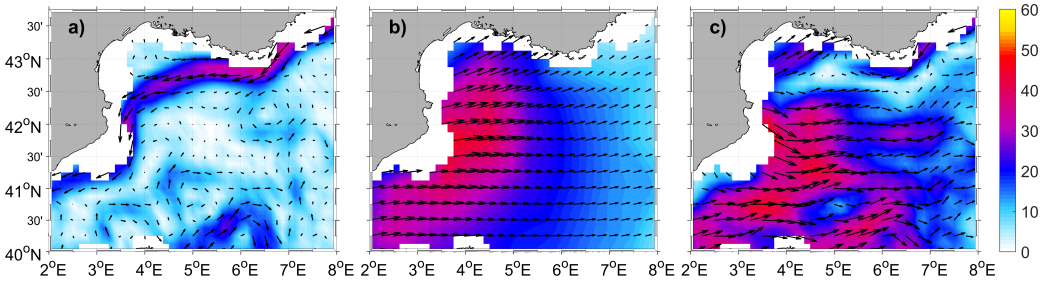

Figure 5. Zoom at the Liguro-Provençal current for a) Geostrophic, b) Ekman and c) Total velocity fields for February the 5th of 2014 at 6:00 UTC. The magnitudes (module, in cm/s) of each velocity component are displayed as background colors according to the color-scale. The black arrows represent the direction of the velocity fields.

$\mathbf{U_{ES}}$ usually have opposite direction with the same order of magnitude, with a minor impacts on the total current. This is particularly appreciable when the Ekman layer is deeper than the Coriolis-Stokes depth ($\delta_s \ll \delta_e$), i.e. under short wave periods, where the effect on the current profile resembles the traditional pure Ekman solution (Polton et al., 2005).

These dynamical conditions associated with a large contribution of the wind and waves induced currents are not isolated cases since these ageostrophic circulation patterns occur frequently over different Mediterranean regions.

5.1 Regionalizing the impacts of wind and waves on the total surface kinetic energy

To further characterize the regions and time periods for which the total surface dynamics are governed by the Ekman and Stokes components, we perform a coupled SOMs analysis between the absolute value of $\mathbf{U}_T$, $\mathbf{U}_g$, $\mathbf{U}_E$ and $\mathbf{U}_S$. Note that these magnitudes are closely related to the root-squared Kinetic Energy (henceforth referred as to KE) given by KE=$(u^2+v^2)^{1/2}$. We first apply the SOM algorithm to the 6-hour velocities for 2005, since this year presents maximum averaged values for the ageostrophic velocities and the areas influenced by each velocity component can be more clearly delimited.

The different temporal pattern extracted from the SOM analysis using a 2x3 neural network in the time domain are shown in Fig. 6 for each of the velocity components. As expected, geostrophy dominates the low frequency variations while the Ekman and Stokes components modulate the high frequency signal of the total velocity, including the sub-daily variability (Onink et al., 2019). This high frequency signal shows the highly variable response of the upper layer dynamics to the rapidly evolving waves and wind forcing. In general, $\mathbf{U_g}$ is of the same order of magnitude as $\mathbf{U_T}$, whereas $\mathbf{U_E}$ is about half (or smaller) of $\mathbf{U_T}$'s intensity while $\mathbf{U_S}$ is one order of magnitude smaller than $\mathbf{U_T}$. As observed in Fig. 6, due to the preservation of the topology, the SOM method organizes the patterns in the neural network according to the similarity in the intensity and variability of each velocity components. Patterns showing high contribution of geostrophy are located around the right top corner of the neuronal network (P2 and P3 in Fig. 6), while patterns where the contribution of Ekman and Stokes velocities is large are found at the left-hand side of the neural network (P1 and P4). And between them, there are some intermediary patterns (P5 and P6). As revealed by some patterns, the wind and waves induced currents are more intense during winters, exceeding the value of the geostrophic

component in some patterns (i.e. P1, P4 and P5). This suggests a strong seasonal variability in the ageostrophic signal which is further analyzed in section 5.2.1.

Fig. 7 shows the objective classification of the Mediterranean Sea in sub-regions based on the combined variability of total, geostrophic, Ekman and Stokes velocity components given by the temporal patterns described previously (Fig. 6). The region where the Ekman and Stokes components have the largest values (R1) corresponds to the temporal pattern P1. It identifies the northern and central sub-basins of the western Mediterranean as a region whose surface dynamics is largely affected by the wind and waves induced currents. It is indeed dominated by strong regional winds (i.e. 'mistral' and 'tramontane') blowing southward with the marine origin in the Gulf of Lion (Zecchetto & De Biasio, 2007; Obermann et al., 2018), where waves can be developed through the large fetch (Sayol et al., 2016; Morales-Márquez et al., 2020). This kind of winds although are stronger with longer duration and more frequent in winter, they also take place in summer (Soukissian et al., 2018). Surprisingly, we found in P1 the events with the larger values of $\mathbf{U_T}$ with velocities up to 40cm/s during the 19^{th} of January, the 14^{th} of February, the 11^{th} of April and the 17^{th} of December (although not easily appreciable in Fig. 6 since the original temporal pattern has been smoothed). Regarding the eastern and central parts of the basin, the influence of the Ekman and Stokes components is higher in the regions R4, R5 and R6, characterized by patterns P4, P5 and P6 (see green, yellow and orange regions in Fig. 7). These patterns can be associated with local winds such as, etesian and bora (Zecchetto & De Biasio, 2007), that although they do not have enough distance without any obstacle in order to the waves to be developed, they are able to cause a large Ekman velocity. Comparing the amplitude of Ekman and Stokes components over all the regions, we can observe that western basin is the region most impacted by wind and waves of the Mediterranean Sea, since there is a larger fetch.

Regions where the dynamics is mainly modulated by the geostrophy (low frequency signal) are characterized by P2 and P3 (Fig. 6) and shown by R2 and R3 in Fig. 7. They identify the well-known geostrophic circulation features in the Mediterranean Sea including the Alboran gyres, Levantine gyres and the detachment of eddies from the Algerian current through baroclinic instability (R2). Indeed, the Algerian current, which flows along the northern African shelf and then crosses the Strait of Sicily towards the southern Ionian Sea, is clearly identified by R3. It is also remarkable how the main Mediterranean gyres are well characterized within the same region (R2), showing a similar variability in the total kinetic energy of this geostrophic features between the western and eastern basins. These temporal patterns also identify the Liguro-Provençal current that is interrupted in the Gulf of Lions due to the effect of the Ekman and Stokes components (R1). Pattern P3 shows an increase of $\mathbf{U_T}$ during August and September, likely due to the importance of the geostrophic component (in contrast to the weakening of wind and waves). P4 characterizes the regions R4 (green areas in Fig. 7) associated with lower total kinetic energy (small values of $\mathbf{U_T}$) and where the Ekman component is relative large, dominating the total velocity during winter season. This pattern identifies broad areas across the western and central parts of the Mediterranean Sea (Thyrrhenian, Adriatic, northern Ionian, Gulf of Gabes and Ebro shelf), as well as small regions around Cyprus (eastern basin). P5 and P6 are exclusive for the central and eastern Mediterranean, respectively; exhibiting intermediate values of Ekman and Stokes velocities, being higher the contribution of the geostrophy and the total kinetic energy in the easter region (R6). It is worth mentioning that, the characteristic map of regions shown in Fig. 7 is in agreement with the main features of the surface dynamics in the Mediterranean Sea outlined in Millot (2005).

5.2 Regional assessment of the temporal variability

In this Section, we extend the analysis to the 25 years of data to assess the role of wind and waves at the inter-annual scale. Each velocity component is spatially averaged

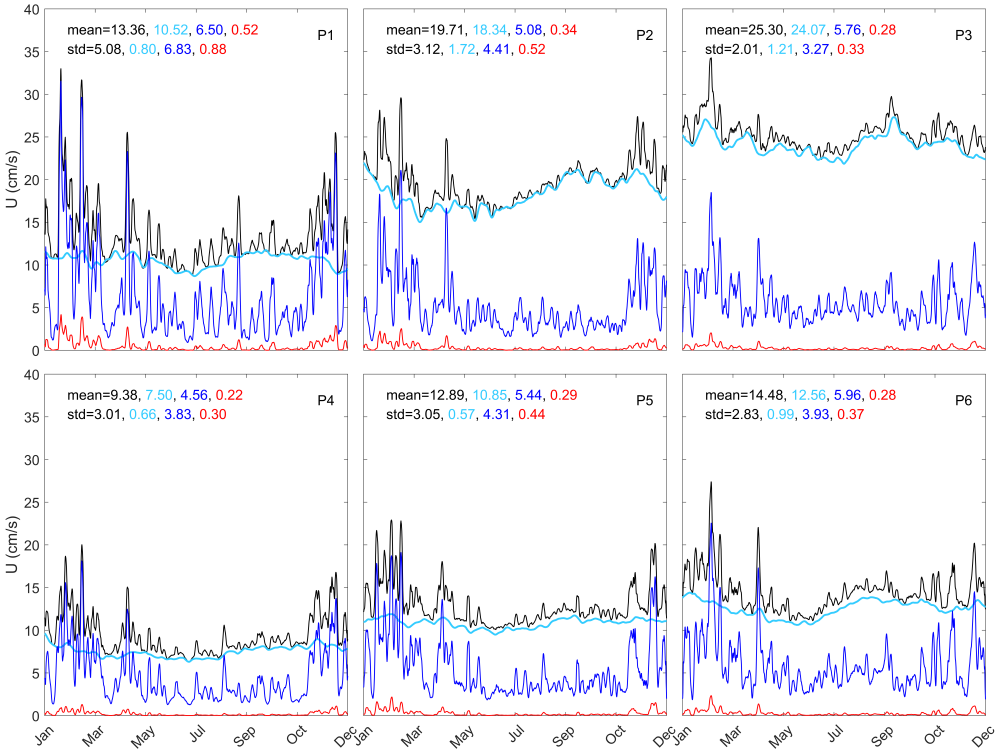

Figure 6. Temporal patterns of the absolute value of the total (black line), geostrophic (cyan line), Ekman (blue line) and Stokes (red line) velocity component fields extracted from the coupled SOMs technique for 2005. Patterns have been smoothed using a moving window of 3.5 days in order to facilitate comparison. The means and the standard deviations of each temporal pattern reported within each panel.

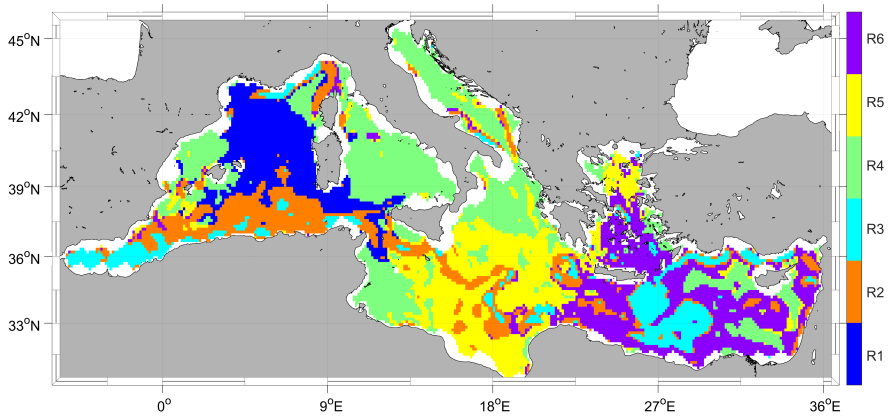

Figure 7. Regions unveiled from the SOM analysis according to the coupled variability of the absolute value of each velocity field component. R1 is dominated by the ageostrophic component; R2/R3, by the geostrophic one and R4/R5/R6 are intermediate patterns.

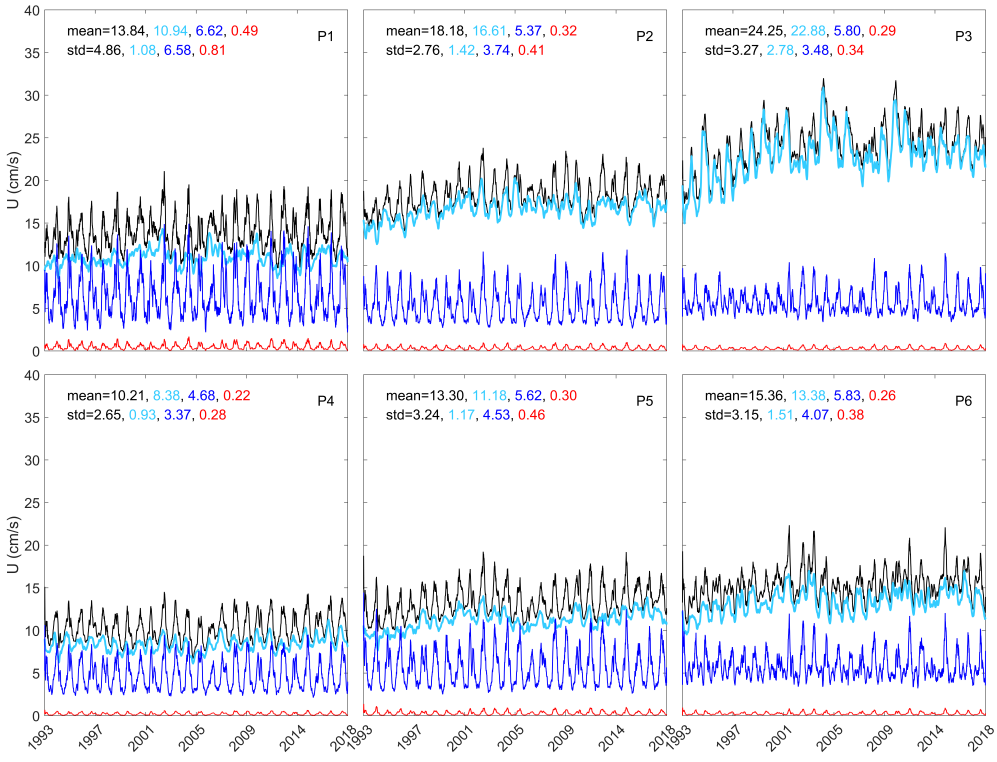

Figure 8. Mean total (black line), geostrophic (cyan line), Ekman (blue line) and Stokes (red line) velocity component module fields from 1993 to 2018 in the regions of the temporal SOMs of 2005.

every 6-h from 1993 to 2018 over each region identified by the previous SOM analysis (Fig. 7) to obtain the time-series reported in Fig. 8. The time series have been smoothed with a moving window of 45 days to improve readability. The different components exhibit similar variability than previously analysed for 2005, with geostrophy clearly dominating in patterns P2 and P3, and with the wind and wave induced velocities being prominent in pattern P1. The geostrophic component appears as the main contributor describing the large scale variability while Ekman and Stokes components incorporate the high frequency and a clear seasonal signal to the total velocity. Despite the fact that the values of Ekman and Stokes velocities are high during short time periods, they impact significantly on the total kinetic energy throughout the entire period analyzed. As seen in pattern P1, the Ekman component surpasses the geostrophy during winter. A similar situation occurs in R4, where the P4 presents smaller total kinetic energy with a large impact of the Ekman component in winter. In the central (R5) and eastern (R6) regions, the geostrophic velocities are larger than the Ekman and Stokes components except for a few occasional events, when the two latter are higher than the former. In general, the contribution of the Ekman component to the total velocity is larger in the central part (P5) than in the eastern one (P6). The effect of Ekman and Stokes components at the eastern part, P6, is particularly significant during 2002, 2012 and 2015 winters (see Fig. 8).

5.2.1 Short-term variability: annual and semiannual cycles

An assessment of the temporal variability (i.e. dominant frequency bands as a function of time) of the different velocity components in each of the SOM regions identified in Fig. 7 is here performed applying a wavelet analysis to their corresponding temporal patterns (Fig. 9). All the regions show a strong seasonal signal (1 year characteristic period) for all the velocities except for the geostrophic component in R1. This strong intra-annual variability is mainly fueled by the ageostrophic components. While in regions R1, R2, R5 and R6 the annual geostrophic signal is interrupted, the Ekman and Stokes components contribute largely to the short term variability (annual cycle) of the total kinetic energy during these 25 years, as indicated by the marked seasonality of Ekman and Stokes components for the entire Mediterranean Sea (Fig. 8). It should be noted that $\mathbf{U_T}$ also exhibits an important semi-annual cycle in R6, and in R3 to a lesser extent, during almost all 25 years except 1999. This characteristic period is also present in geostrophy but more discontinued than in the ageostrophic velocity. Note that the semi-annual signal in the geostrophic current in R1 from 2000 to 2008 is removed in the total velocity.

5.2.2 Long-term variability: relation with climatic modes of variability

Long-term oscillations are found in the total velocity with characteristics periods of around 2, 3 and 5 - 6 years over the whole basin. The long term variability on the total velocity field is modulated by the geostrophic component in all the regions. However, Ekman and Stokes components increase the spectrum power of these characteristics periods in some regions. In the western Mediterranean (R1), additional significant periods are identified around 2 and 3 years from 2010 to 2017, from 1999 to 2006 and from 2008 to 2013, respectively, as a result from the combination of the geostrophic and ageostrophic variability. As already suggested in Fig. 8, the Ekman component dominates the variability in this region during the 25 years period. In R2, there are significant signals with periods of 1.5 - 2 years and 2 - 4 years over 2013 - 2018 and 2001 - 2015, respectively, also due to the combined influences of the different velocity components. On the other hand, $\mathbf{U_g}$ in R3 is practically the main contributor to the 1.5 - 2 years and 4 - 6 years cycles in the total velocity. Therefore $\mathbf{U_a}$ has poor relevance in explaining the long-term variability in this region. Regions R4 and R5 present a 4 - 6 year-period well defined and a 1.5 years period in some specific years (see Fig. 9, R4 and R5). In R5, the annual signal is intermittent in $\mathbf{U_g}$ being present during the 25 years in $\mathbf{U_a}$. Finally, $\mathbf{U_T}$ in R6 registers cycles of 1 - 2.5 years and 1.5 years during 1997 - 2003 and 2013 - 2018, respectively. Periods ranging 5 to 6 years coincide with the characteristic periods of the dominant climatic patterns of variability acting over the Mediterranean Sea (Morales-Márquez et al., 2020).

In order to get insights about the regional influence of the modes of atmospheric variability on the upper layer dynamics in the Mediterranean Sea, we perform a wavelet coherence analysis between the NAO, EA, EA/WR and SCAND indices and the $\mathbf{U_T}$ in the dynamical regions previously identified (Fig. 10). This method allows identifying the frequency bands within which time series of KE for each SOMs region and the large scale atmospheric forcings co-vary.

NAO is correlated with the total velocity with signals of around 1 year during 2014 to 2018 in all the SOM regions (see Fig. 10, NAO). For periods spanning 5 - 7 years the total velocity signal is anticorrelated with the NAO in all regions except R1 where the negative correlation is around 2.5 years. Note that R1 corresponds to the region where wind and waves are most relevant for the modulation of the high frequency variability of the total currents. This is in agreement with the results obtained by Morales-Márquez et al. (2020) where a strongly significant anticorrelation between extreme waves and the

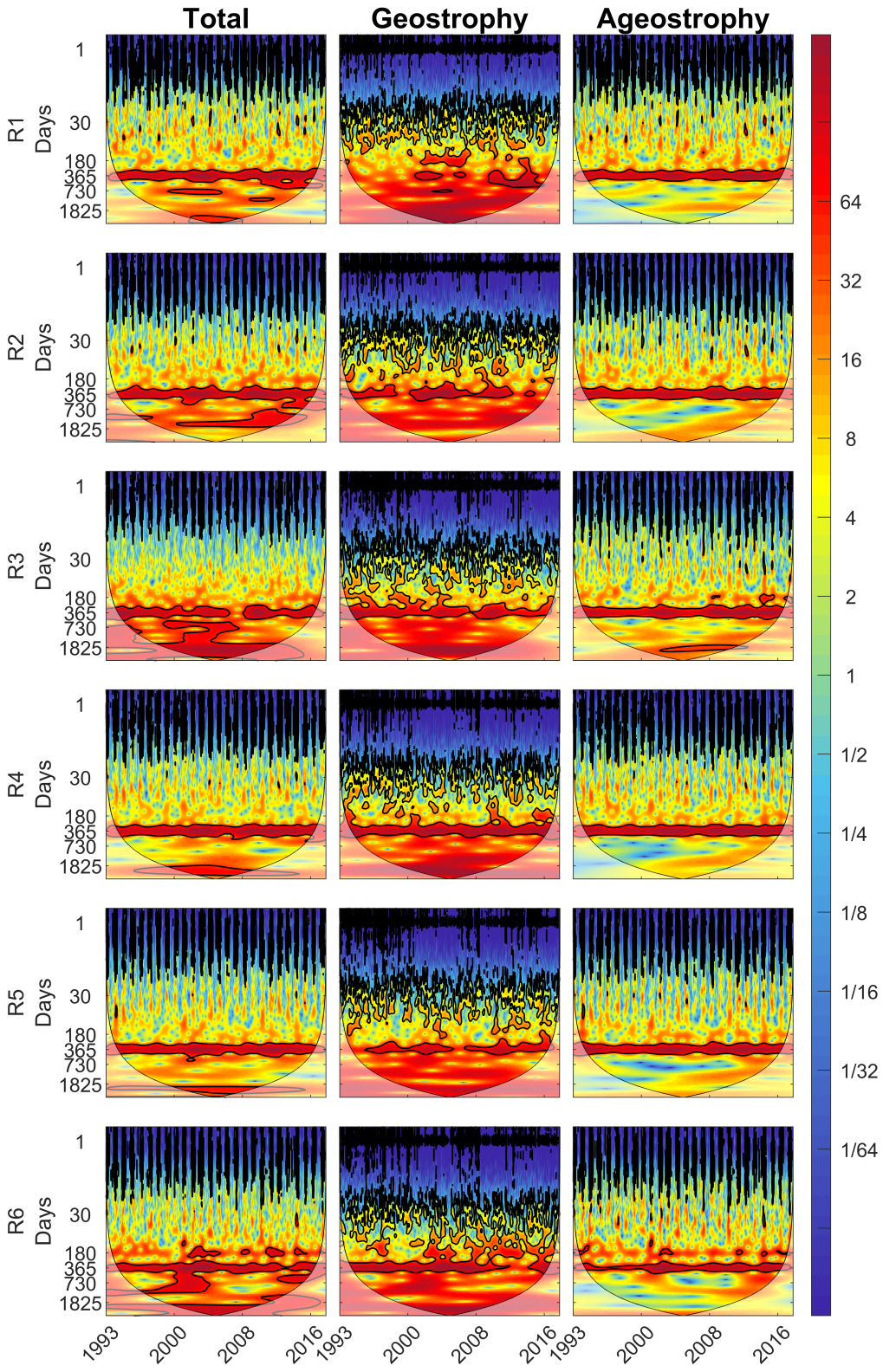

Figure 9. Wavelet power spectrum of the 6-hours time series of the spatially-averaged (over the SOM regions shown in Fig. 8) Total, Geostrophic and Ageostrophic velocity components from 1993 to 2018. Contours in black indicates the 95% significant levels. Lighter shades show the cone of influence (COI) where the edge effects may distort the Fourier analysis.

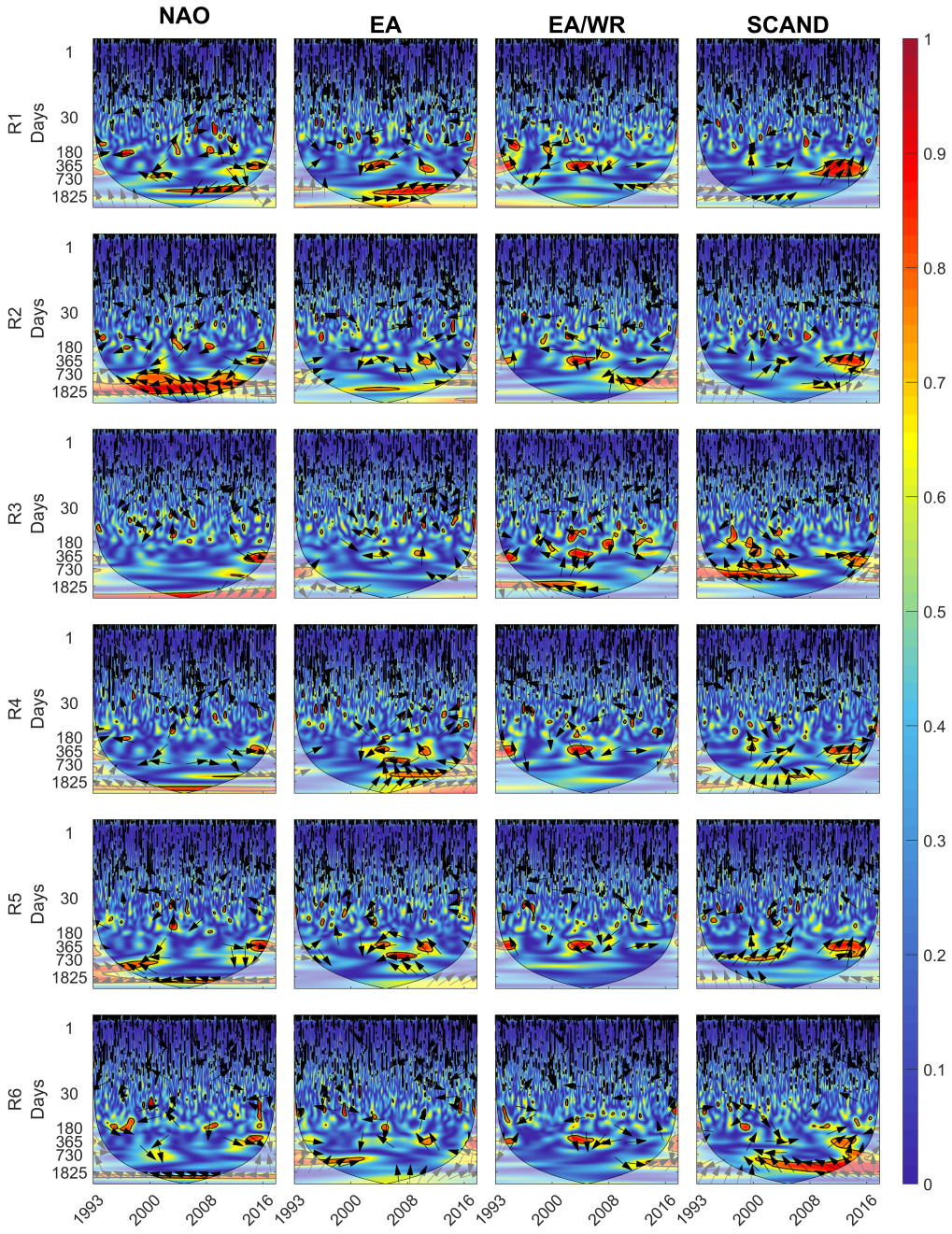

Figure 10. Wavelet coherence between the mean total velocity module for temporal 2005 SOMs patterns and the monthly values of NAO, EA, EA/WR and SCAND climatic indices from 1993 to 2018. The arrows determine the phase between both series. Arrows pointing to the right represent positive correlation (signals in phase) and when they point to the left, anti-correlation (signals in anti-phase). Contours indicate wavelet squared coherence.

NAO was obtained in the Mediterranean Sea. NAO has a significant influence in R2 with a negative correlation at 2- 5 years during the period of analysis, and in R5 with negative correlation around 2 - 4 years from 1993 to 2002. In addition, NAO has an effect on the semiannual variability in all regions during 1996, 2003 and 2008 being less visible in R3 and R5 (see Fig. 10, NAO).

The influence of EA on the variability of the total current in R1 and R4 is associated with 1.5 and 4 - 5 years signals after 2000 (see Fig 10, EA). In R1, correlation occurs between 2003 to 2016 with a 4 year-period and for the 25 years period around 7 years (see Fig. 10, R1, EA). Similar but less intense atmospheric influence is found in R5 and R6. In all regions a strong anticorrelation is shown around 1 year from 2002 to 2005 and from 2016 to 2018. EA also affects R4 and R5 with a 2 years signal between 2009 to 2012. Note that EA does not affect R3, that is where mesoscale surface dynamics is mainly controlled by the geostrophic component. R6 shows a positive correlation with the EA 3 year-period from 1993 to 2002.

The signature of the 1 year signal, associated with EA/WR, is clearly seen in all the Mediterranean surface dynamics between 2003 to 2005. The western Mediterranean (R1 and R2) shows an anticorrelation with EA/WR signals at 4 year-period from 2010 to 2018, and around 5-year period in R3 from 1993 to 2007, in agreement with the relationships documented for extreme waves by Morales-Márquez et al. (2020).

The influence of SCAND index on total surface currents manifests itself with a positive correlation at 1 - 2-year period for the whole basin after 2006. The impact of SCAND climate mode is more intense in Eastern Mediterranean as shown by the negative/positive correlation in the 1.5 - 3 years band between 1993 and 2006 in R3/R5 and by the strong negative correlation around 3 - 5 year-period during 2000 - 2018 in R6.

5.2.3 Trends in the Kinetic Energy

To analyze linear trends in the geostrophic and total velocity modules, the residual of $\mathbf{U_T}$ and $\mathbf{U_g}$ are fitted by a linear regression in time at each spatial point (see Fig. 11). We have verified these results with the Theil Sean estimator technique, obtaining similar trend patterns (not shown). The significance level is set at 90% with the Mann Kendall method and with a t-value adjusted of $N-2$ degrees of freedom (Pastor et al., 2018), being the number of points with no-significant values slightly larger using the Mann Kendall method. The estimated global Mediterranean trend of total speed is positive with a value of 0.058 $\pm$1.43 10^{-5} cm/s per year, being the geostrophic one higher with a value of 0.063 $\pm$1.20 10^{-5} cm/s per year (see Fig. 11). It suggests that surface velocities, and associated KE, are increasing over this 25 years period. While regions where the wind- and wave-induced velocities have the largest impacts (R1 and R4) do not exhibit clear and significant trends in the total velocity module (not shown), the geostrophic dominated regions (R3 and R2) show positive trends with a shift in 2003 (0.59 $\pm$8.15 10^{-5} and 0.37 $\pm$6.56 10^{-5} cm/s per year), see Fig. 12. These results are consistent with the KE increase presented in Ser-Giacomi et al. (2020), they explain this rise as a potential relation to an increment of a baroclinic instability since they show a decrease of the wind stress across the most of the western basin. While such mechanism could also explain the rising trend evidenced here, further analyses are needed to ascertain which mechanism is at play. Note however that the clear positive trend from 1993 to 2002 seems to slow down after 2003. It could indicate that this is not a proper trend but rather part of a longer oscillation or an artifact due to the inconsistency in the SLA dataset of 25 years. However the altimeter product used in this study (see section 3) is the result of homogenization procedure among several altimeter satellite observations and is thus considered suitable for trend analysis (Pujol et al., 2016). $\mathbf{U_T}$ and $\mathbf{U_g}$ present similar trends during the 25 years analyzed (see Fig. 11, a and b) with an increment in the eastern Mediterranean Sea and a decrease in the western basin. The global trend is generally positive

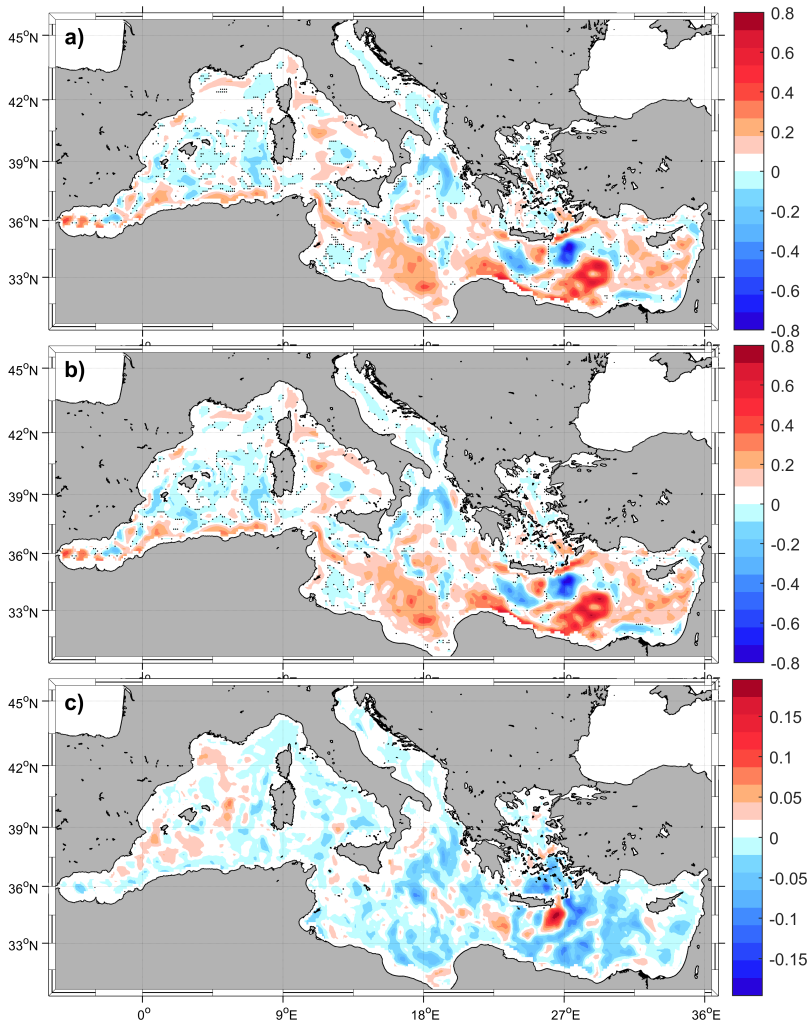

Figure 11. Trend of the a) Total velocity module and b) Geostrophic component module from 1993 to 2018 in cm/s per year. c) Difference between a) and b). No significant values at the 90% confidence interval are dotted (with Mann Kendall method).

in regions where the geostrophy is dominant, except in the Libyan Sea where both $\mathbf{U_T}$ and $\mathbf{U_g}$ tendencies are negative, in good agreement with Fig. 8. The maximum trend of 0.72 $\pm$2.44 10^{-5} cm/s per year for $\mathbf{U_T}$ is found in the eastern part of the Mediterranean basin. In contrast, the minimum value in the Libyan Sea is -0.81 $\pm$2.42 10^{-5} cm/s per year (Fig.11, a). The maximum and minimum trends for $\mathbf{U_g}$ are found in the same regions with slightly smaller values, 0.73 $\pm$2.20 10^{-5} and -0.77 $\pm$2.85 10^{-5} cm/s per year, (Fig.11, b). The ageostrophic input on the trend of the total velocity module is evaluated through the difference between both tendencies, $\mathbf{U_T}$ and $\mathbf{U_g}$). Most values are close to zero in the whole Mediterranean (see Fig.11, c), except in the region with the minimum trend of $\mathbf{U_T}$ where the difference of trends is $\sim$ 0.2 $\pm$9.89 10^{-7} cm/s per year. In the western region, there are some areas with a small positive differences of trend of 0.05 $\pm$6.33 10^{-7} cm/s per year, corresponding to R1 of Fig. 7 and also to the regions of the main regional winds.

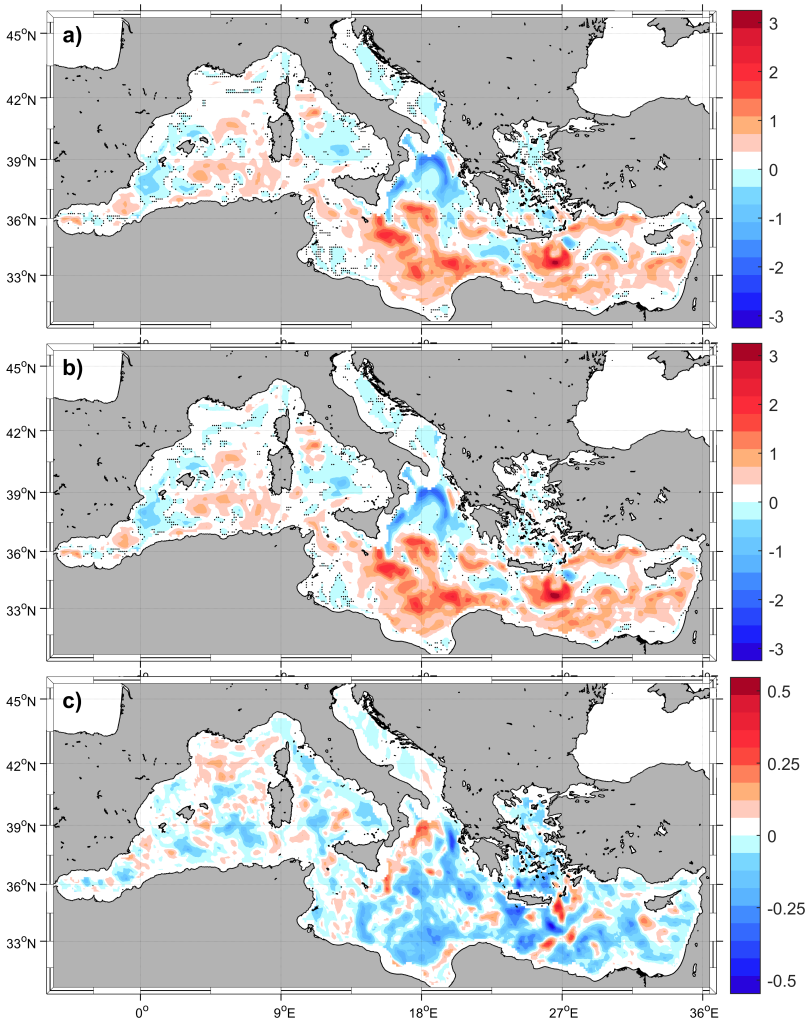

Figure 12. Trend of the a) Total velocity module and b) Geostrophic component module from 1993 to 2002 in cm/s per year. c) Difference between a) and b). No significant values at the 90% confidence interval are dotted (with Mann Kendall method).

Positive global trends of other oceanic variables have also been observed for the Mediterranean. (Pujol & Larnicol, 2005) reported a trend in the root squared Eddy Kinetic Energy of 0.7 cm/s per year, between 1993 and 2003, and (Pastor et al., 2018) showed a linear trend for Sea Surface Temperature from 1982 to 2016 of 0.03 $\pm$ 0.003 ^{o}C per year.

6 Conclusions

This study analyzes the effect of Ekman and Stokes velocities on the total kinetic energy in the upper layer of Mediterranean Sea. By solving the momentum equation (Eq. 4) we include the interaction between Ekman and Stokes drift on the geostrophic velocity. Total velocity is decomposed into different components: the geostrophic, Ekman, Stokes and the interaction between Ekman and Stokes. The regional relevance of these different components is evaluated through SOM decomposition, and their variability through wavelet analysis.

Once the velocity components are obtained, a dynamical regionalization of the Mediterranean Sea has been performed based on the local impacts of waves and wind on the total velocity variability. Ekman currents account for the short-term variability (seasonal, semi-seasonal and smaller time scales) of the surface circulation, especially during winter when the Ekman component occasionally exceeds geostrophy due to strong regional winds. The regionalization shows that the effects of Ekman and Stokes are more marked in the western than in the eastern Mediterranean basin. This is the result of the larger fetch in the western basin, allowing the development of larger swells (Mao & Heron, 2008). Regionalization of velocity components identifies two regions (associated with the main Mediterranean gyres and the Algerian current) where the geostrophy modulates the total kinetic energy variability. These regions are characterized by a positive trend of the module velocity of 0.14 $\pm$2.15 10^{-5} cm/s per year during the 25 years, with stronger increments during 1993$-$2002. The dominant periods of the total currents in the entire Mediterranean Sea, essentially dominated by geostrophy, are 1 and 5 - 6 years. In regions where the inclusion of both Ekman and Stokes velocities returns a significantly different flow field than the one obtained by geostrophic approximation, intermediate periodicity values between 1 and 5 years are found. These signals of variability are related with the principal climatic modes typical of the Mediterranean basin: the NAO, EA EA/WR and SCAND patterns. NAO dominates, with a negative correlation, the large-scale, around 5 - 7 years in the whole basin except in the western Mediterranean, which was already noticed by Morales-Márquez et al. (2020). Furthermore, NAO is correlated with the annual variability during 2014-2018 and with the semiannual variability at the whole basin, although these connections are weaker for geostrophy-dominated region. The EA index has a positive large-scale correlation in the Mediterranean Sea (4 - 7 years), with the exception of the geostrophic modulated region. The long-term variability effect of EA/WR on the currents velocity is negative and between periods of 4 to 5 years, in particular in the Western Mediterranean. Finally, the SCAND mode of variability has a negative effect in periods of 3 -5 years in the eastern basin.

The methodology presented in this work can be used to better understand the physical, biological and chemical processes occurring at the upper layers of any ocean region using only observations with a low computational cost. In the Mediterranean Sea, there is a need for an improved wave model accounting for the feedback between the Ekman currents on the wave field evolution, and how the Ekman layer evolves due to the nonlinear evolution of the wave field, which necessarily contemplates a non-steady Ekman current, as shown in Shrira and Almelah (2020). Next step is devoted to extend this analysis to study transport properties from the Lagrangian point of view. Thus, several applications (e.g. floating debris, oil spill, Search and Rescue, jellyfish tracking, etc.) could benefit from this approach to obtain reliable nowcast.

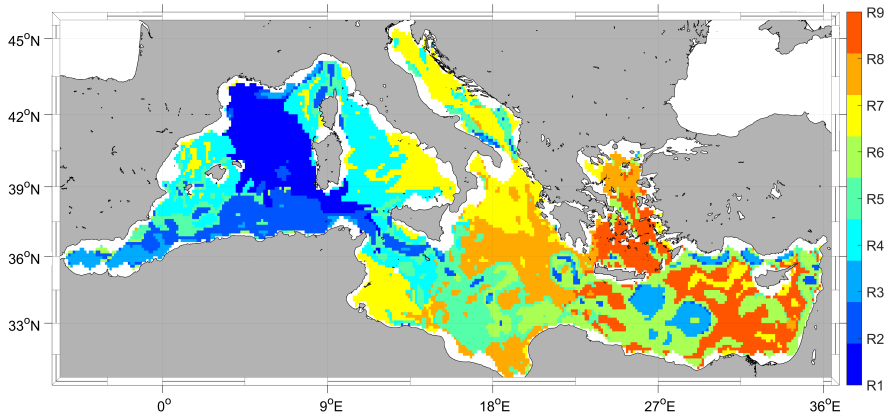

Figure A1. Temporal patterns of the absolute value of the total (black line), geostrophic (cyan line), Ekman (blue line) and Stokes (red line) velocity component fields extracted from the coupled SOMs technique for 2005 with 9 neurons.

Appendix A Supplementary material

Acknowledgments

Authors acknowledge financial support from MINECO/FEDER through projects MOCCA (RTI2018-093941-B-C31) and from the Balearic Islands Goverment Project ADAPTA. V. Morales-Márquez is supported by an FPI grant from the Ministerio de Ciencia, Innovación y Universidades. I. Hernandez-Carrasco acknowledges the Vicenç Mut contract funded by the Government of the Balearic Island and the European Social Fund (ESF) Operational Programme and the financial support from the Fundacion Universidad Empresa de las Islas Baleares, Spain through project ALERTA (REF-190121). V. Rossi acknowledges financial support from the European project SEAMoBB, funded by ERA-Net Mar-TERA and managed by ANR (number ANR_17_MART-0001_01, P.I.: A.C.). This work was partially performed while V. Morales-Márquez was staying in MIO (Marseille, France) with the support of FPI grant from the Ministerio de Ciencia, Innovación y Universidades. In addition, this work was carried out in part when A. Orfila was a visiting scientist at the Earth, Environmental and Planetary Sciences Department at Brown University through a Ministerio de Ciencia, Innovación y Universidades fellowship (PRX18/00218). All data are accessible from `https://apps.ecmwf.int/datasets/data/interim-full-daily/levtype=sfc/`, `fromhttps://www.cpc.ncep.noaa.gov/data/teledoc/telecontents.shtml` and from `https://resources.marine.copernicus.eu/?option=com_csw&view=details&product_id=SEALEVEL_MED_PHY_L4_REP_OBSERVATIONS_008_051`.

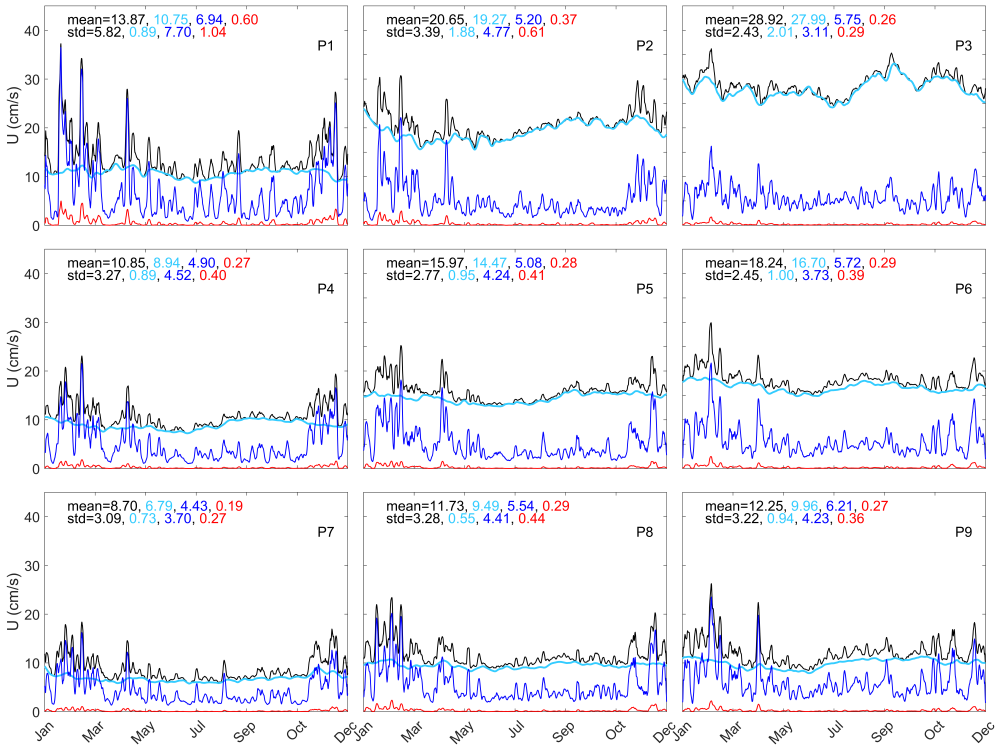

Figure A2. Regions unveiled from the SOM analysis, with 9 neurons, according to the coupled variability of the absolute value of each velocity field component.

References

Ardhuin, F., Aksenov, Y., Benetazzo, A., Bertino, L., Brandt, P., Caubet, E., ... Xie, J. (2018). Measuring currents, ice drift, and waves from space: the Sea surface KInematics Multiscale monitoring (skim) concept. *Ocean Science*, *14*(3), 337–354.

Ardhuin, F., Marié, L., Rascle, N., Forget, P., & Roland, A. (2009). Observation and estimation of Lagrangian, Stokes, and Eulerian currents induced by wind and waves at the sea surface. *Journal of Physical Oceanography*, *39*(11), 2820–2838.

Ayata, S.-D., Irisson, J.-O., Aubert, A., Berline, L., Dutay, J.-C., Mayot, N., ... Guineu, C. (2018). Regionalisation of the Mediterranean basin, a MERMEX synthesis. *Progress in Oceanography*, *163*, 7–20. doi: https://doi.org/10.1016/j.pocean.2017.09.016

Barnston, A. G., & Livezey, R. E. (1987). Classification, seasonality and persistence of low-frequency atmospheric circulation patterns. *Monthly Weather Review*, *115*(6), 1083–1126.

Berrisford, P., Dee, D., Poli, P., Brugge, R., Fielding, K., Fuentes, M., ... Simmons, A. (2011). *The ERA-Interim archive, version 2.0* (Tech. Rep.). ECMWF.

Bourassa, M. A., Meissner, T., Cerovecki, I., Chang, P., Dong, X., De Chiara, G., ... others (2019). Remotely sensed winds and wind stresses for marine forecasting and ocean modeling. *Frontiers in Marine Science*, *6*, 443. doi: https://doi.org/10.3389/fmars.2019.00443

Breivik, Ø., Bidlot, J.-R., & Janssen, P. A. (2016). A Stokes drift approximation based on the Phillips spectrum. *Ocean Modelling*, *100*, 49–56.

Bronselaer, B., & Zanna, L. (2020). Heat and carbon coupling reveals ocean warming due to circulation changes. *Nature*, *584*(7820), 227–233. doi: https://doi.org/10.1038/s41586-020-2573-5

Covey, C., & Barron, E. (1988). The role of ocean heat transport in climatic change. *Earth-Science Reviews*, *24*(6), 429–445. doi: https://doi.org/10.1016/0012-8252(88)90065-7

Daubechies, I. (1990). The wavelet transform, time-frequency localization and signal analysis. *IEEE transactions on information theory*, *36*(5), 961–1005.

Dee, D. P., Uppala, S. M., Simmons, A., Berrisford, P., Poli, P., Kobayashi, S., ... others (2011). The ERA-Interim reanalysis: Configuration and performance of the data assimilation system. *Quarterly Journal of the royal meteorological society*, *137*(656), 553–597. doi: https://doi.org/10.1002/qj.828

Dobler, D., Huck, T., Maes, C., Grima, N., Blanke, B., Martinez, E., & Ardhuin, F. (2019). Large impact of Stokes drift on the fate of surface floating debris in the South Indian Basin. *Marine pollution bulletin*, *148*, 202–209. doi: https://doi.org/10.1016/j.marpolbul.2019.07.057

d'Ortenzio, F., & d'Alcalà, M. R. (2009). On the trophic regimes of the Mediterranean Sea: a satellite analysis. *Biogeosciences*, *6*(2).

Dubois, M., Rossi, V., Ser-Giacomi, E., Arnaud-Haond, S., López, C., & Hernández-García, E. (2016). Linking basin-scale connectivity, oceanography and population dynamics for the conservation and management of marine ecosystems. *Global Ecology and Biogeography*, *25*(5), 503–515. doi: doi:10.1111/geb.12431

Ekman, V. W. (1905). On the influence of the Earth's rotation on ocean-currents. *Arkiv for Matematik, Astronomi, och Fysik*, *2*(11), 1–53.

Fraser, C. I., Morrison, A. K., Hogg, A. M., Macaya, E. C., van Sebille, E., Ryan, P. G., ... Waters, J. M. (2018). Antarctica's ecological isolation will be broken by storm-driven dispersal and warming. *Nature climate change*, *8*(8), 704–708. doi: https://doi.org/10.1038/s41558-018-0209-7

Futch, V. C., & Allen, A. (2019). Search and rescue applications: on the need to improve ocean observing data systems in offshore or remote locations. *Frontiers in Marine Science*, *6*, 301.

Grinsted, A., Moore, J. C., & Jevrejeva, S. (2004). Application of the cross wavelet transform and wavelet coherence to geophysical time series. *Nonlinear Processes Geophysics*, *11*, 561–566. doi: 10.5194/npg-11-561-2004

Hernández-Carrasco, I., & Orfila, A. (2018). The Role of an Intense Front on the Connectivity of the Western Mediterranean Sea: The Cartagena-Tenes Front. *Journal of Geophysical Research: Oceans*, *123*(6), 4398–4422. doi: 10.1029/2017JC013613

Hernández-Carrasco, I., Rossi, V., Hernández-García, E., Garçon, V., & López, C. (2014). The reduction of plankton biomass induced by mesoscale stirring: A modeling study in the benguela upwelling. *Deep Sea Research Part I: Oceanographic Research Papers*, *83*, 65–80. doi: 10.1016/j.dsr.2013.09.003

Huang, N. E. (1979). On surface drift currents in the ocean. *Journal of Fluid Mechanics*, *91*(1), 191–208.

Hui, Z., & Xu, Y. (2016). The impact of wave-induced Coriolis-Stokes forcing on satellite-derived ocean surface currents. *Journal of Geophysical Research: Oceans*, *121*(1), 410-426. doi: 10.1002/2015JC011082

Hurrell, J. W., Kushnir, Y., Ottersen, G., & Visbeck, M. (2003). An overview of the North Atlantic oscillation. *The North Atlantic Oscillation: climatic significance and environmental impact*, 1–35.

Janssen, P. A., Hansen, B., & Bidlot, J.-R. (1997). Verification of the ECMWF wave forecasting system against buoy and altimeter data. *Weather and Forecasting*, *12*(4), 763–784.

Kaiser, G. (1994). A Friendly guide to wavelets: Basic wavelet analysis, physical wavelets. *Birkhauser*, 300.

Kohonen, T. (1982). Self-organized formation of topologically correct feature maps. *Biological cybernetics*, *43*(1), 59–69.

Large, W. G., McWilliams, J. C., & Doney, S. C. (1994). Oceanic vertical mixing: A review and a model with a nonlocal boundary layer parameterization. *Reviews of Geophysics*, *32*(4), 363–403.

Lewis, D., & Belcher, S. (2004). Time-dependent, coupled, Ekman boundary layer solutions incorporating Stokes drift. *Dynamics of atmospheres and oceans*, *37*(4), 313–351.

Liu, Y., Weisberg, R. H., & Mooers, C. N. (2006). Performance evaluation of the self-organizing map for feature extraction. *Journal of Geophysical Research: Oceans*, *111*(C5).

Mao, Y., & Heron, M. L. (2008). The influence of fetch on the response of surface currents to wind studied by HF ocean surface radar. *Journal of physical oceanography*, *38*(5), 1107–1121.

McWilliams, J. C., Gula, J., Molemaker, M. J., Renault, L., & Shchepetkin, A. F. (2015). Filament frontogenesis by boundary layer turbulence. *Journal of Physical Oceanography*, *45*(8), 1988–2005.

McWilliams, J. C., & Restrepo, J. M. (1999). The wave-driven ocean circulation. *Journal of Physical Oceanography*, *29*(10), 2523–2540.

McWilliams, J. C., Sullivan, P. P., & Moeng, C.-H. (1997). Langmuir turbulence in the ocean. *Journal of Fluid Mechanics*, *334*, 1–30.

Millot, C. (2005). Circulation in the Mediterranean Sea: evidences, debates and unanswered questions. *Scientia marina*, *69*(S1), 5–21.

Morales-Márquez, V., Orfila, A., Simarro, G., & Marcos, M. (2020). Extreme waves and climatic patterns of variability in the Eastern North Atlantic and Mediterranean basins. *Ocean Science*, *16*, 1385—1398.

Nieblas, A.-E., Drushka, K., Reygondeau, G., Rossi, V., Demarcq, H., Dubroca, L., & Bonhommeau, S. (2014). Defining Mediterranean and Black Sea biogeochemical subprovinces and synthetic ocean indicators using mesoscale oceanographic features. *PloS one*, *9*(10), e111251.

Obermann, A., Bastin, S., Belamari, S., Conte, D., Gaertner, M. A., Li, L., &

Ahrens, B. (2018). Mistral and tramontane wind speed and wind direction patterns in regional climate simulations. *Climate Dynamics*, *51*(3), 1059–1076. doi: https://doi.org/10.1007/s00382-016-3053-3

Onink, V., Wichmann, D., Delandmeter, P., & Van Sebille, E. (2019). The role of Ekman currents, geostrophy, and Stokes drift in the accumulation of floating microplastic. *Journal of Geophysical Research: Oceans*, *124*(3), 1474–1490.

Pastor, F., Valiente, J. A., & Palau, J. L. (2018). Sea surface temperature in the Mediterranean: Trends and spatial patterns (1982–2016). *Pure and Applied Geophysics*, *175*, 4017—4029. doi: https://doi.org/10.1007/s00024-017-1739-z

Pearson, B. (2018). Turbulence-induced anti-Stokes flow and the resulting limitations of Large-Eddy simulation. *Journal of Physical Oceanography*, *48*(1), 117–122.

Phillips, O. M. (1966). *The dynamics of the upper ocean.* CUP Archive.

Polton, J. A., Lewis, D. M., & Belcher, S. E. (2005). The role of wave-induced Coriolis–stokes forcing on the wind-driven mixed layer. *Journal of Physical Oceanography*, *35*(4), 444–457.

Pujol, M.-I., Faugère, Y., Taburet, G., Dupuy, S., Pelloquin, C., Ablain, M., & Picot, N. (2016). DUACS DT2014: the new multi-mission altimeter data set reprocessed over 20 years. *Ocean Sci*, *12*(5), 1067–1090. Retrieved from `https://os.copernicus.org/articles/12/1067/2016/` doi: 10.5194/os-12-1067-2016

Pujol, M.-I., & Larnicol, G. (2005). Mediterranean Sea eddy kinetic energy variability from 11 years of altimetric data. *Journal of Marine Systems*, *58*(3-4), 121–142. doi: https://doi.org/10.1016/j.jmarsys.2005.07.005

Reygondeau, G., Guieu, C., Benedetti, F., Irisson, J.-O., Ayata, S.-D., Gasparini, S., & Koubbi, P. (2017). Biogeochemical regions of the Mediterranean Sea: an objective multidimensional and multivariate environmental approach. *Progress in oceanography*, *151*, 138–148.

Rio, M.-H., Mulet, S., & Picot, N. (2014). Beyond goce for the ocean circulation estimate: Synergetic use of altimetry, gravimetry, and in situ data provides new insight into geostrophic and ekman currents. *Geophysical Research Letters*, *41*(24), 8918–8925. doi: doi:10.1002/2014GL061773

Roelvink, D., Reniers, A., Van Dongeren, A., De Vries, J. V. T., McCall, R., & Lescinski, J. (2009). Modelling storm impacts on beaches, dunes and barrier islands. *Coastal Engineering*, *56*(11-12), 1133–1152.

Rossi, V., Ser-Giacomi, E., López, C., & Hernández-García, E. (2014). Hydrodynamic provinces and oceanic connectivity from a transport network help designing marine reserves. *Geophysical Research Letters*, *41*(8), 2883–2891.

Sayol, J. M., Orfila, A., & Oey, L.-Y. (2016). Wind induced energy–momentum distribution along the Ekman–Stokes layer. Application to the Western Mediterranean Sea climate. *Deep Sea Research Part I: Oceanographic Research Papers*, *111*, 34–49.

Sayol, J. M., Orfila, A., Simarro, G., Conti, D., Renault, L., & Molcard, A. (2014). A Lagrangian model for tracking surface spills and SaR operations in the ocean. *Environmental Modelling & Software*, *52*, 74–82.

Ser-Giacomi, E., Sánchez, G. J., Soto-Navarro, J., Thomsen, S., Mignot, J., Sevault, F., & Rossi, V. (2020). Impact of climate change on surface stirring and transport in the Mediterranean Sea. *Geophysical Research Letters*, e2020GL089941. doi: https://doi.org/10.1029/2020GL089941

Shrira, V. I., & Almelah, R. B. (2020). Upper-ocean ekman current dynamics: a new perspective. *Journal of Fluid Mechanics*, *887*.

Soukissian, T., Karathanasi, F., Axaopoulos, P., Voukouvalas, E., & Kotroni, V. (2018). Offshore wind climate analysis and variability in the Mediterranean Sea. *International Journal of Climatology*, *38*(1), 384–402. doi: 10.1002/joc.5182

Stokes, G. G. (1847). On the theory of oscillatory waves. *Transactions of the Cambridge philosophical society*, *8*, 441–455.

Sudre, J., Maes, C., & Garçon, V. (2013). On the global estimates of geostrophic and Ekman surface currents. *Limnology and Oceanography: Fluids and Environments*, *3*(1), 1–20. doi: 10.1215/21573689âĂŘ2071927

Torrence, C., & Compo, G. P. (1998). A practical guide to wavelet analysis. *Bulletin of the American Meteorological society*, *79*(1), 61–78. doi: doi:10.1175/1520-0477

Van Sebille, E., Wilcox, C., Lebreton, L., Maximenko, N., Hardesty, B. D., Van Franeker, J. A., ... Law, K. L. (2015). A global inventory of small floating plastic debris. *Environmental Research Letters*, *10*(12), 124006.

Villarino, E., Watson, J. R., Jönsson, B., Gasol, J. M., Salazar, G., Acinas, S. G., ... others (2018). Large-scale ocean connectivity and planktonic body size. *Nature communications*, *9*(1), 1–13. doi: https://doi.org/10.1038/s41467-017-02535-8

Wallace, J. M., & Gutzler, D. S. (1981). Teleconnections in the Geopotential Height Field during the Northern Hemisphere Winter. *Monthly Weather Review*, *109*(4), 784-812. doi: 10.1175/1520-0493

Wenegrat, J. O., & McPhaden, M. J. (2016). Wind, waves, and fronts: Frictional effects in a generalized Ekman model. *Journal of Physical Oceanography*, *46*(2), 371–394.

Zecchetto, S., & De Biasio, F. (2007). Sea surface winds over the Mediterranean basin from satellite data (2000–04): Meso-and local-scale features on annual and seasonal time scales. *Journal of Applied Meteorology and Climatology*, *46*(6), 814–827. doi: DOI:10.1175/JAM2498.1